Hybrid-Basis Close-Coupling Interface to Quantum Chemistry Packages for the Treatment of Ionization Problems

Carlos Marante,[†] Markus Klinker,[†] Inés Corral,[†] Jesús González-Vázquez,*,[†] Luca Argenti,[†] and Fernando Martín*,[†,‡,§]

[†]Departamento de Química, Módulo 13, Universidad Autónoma de Madrid, 28049 Madrid, Spain, EU
[‡]Instituto Madrileño de Estudios Avanzados en Nanociencia (IMDEA-Nanociencia), Cantoblanco, 28049 Madrid, Spain, EU
[§]Condensed Matter Physics Center (IFIMAC), Universidad Autónoma de Madrid, 28049 Madrid, Spain, EU

ABSTRACT: The theoretical description of observables in attosecond pump−probe experiments requires a good representation of the system's ionization continuum. For polyelectronic molecules, however, this is still a challenge, due to the complicated short-range structure of correlated electronic wave functions. Whereas quantum chemistry packages (QCP) implementing sophisticated methods to compute bound electronic molecular states are well-established, comparable tools for the continuum are not widely available yet. To tackle this problem, we have developed a new approach that, by means of a hybrid Gaussian-B-spline basis, interfaces existing QCPs with close-coupling scattering methods. To illustrate the viability of this approach, we report results for the multichannel ionization

of the helium atom and of the hydrogen molecule that are in excellent agreement with existing accurate benchmarks. These findings, together with the versatility of QCPs to describe a broad range of chemical systems, indicate that this is a valid approach to study the ionization of polyelectronic systems in which correlation and exchange symmetry play a major role.
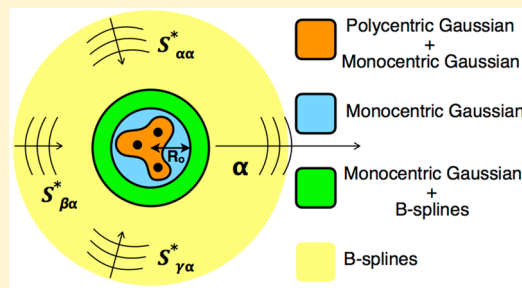
1. INTRODUCTION

Advances in generating controlled few-cycle laser pulses and novel ultrashort extreme ultraviolet (XUV) and X-ray sources, from free-electron laser (FEL)-based to attosecond high harmonic generation (HHG)-based facilities, have opened completely new avenues for imaging and controlling electronic and nuclear dynamics in molecules, with exciting applications in physics, chemistry, and biology.[1−8] The advent of X-ray free-electron lasers (XFEL),[9] has extended the domain of inquiry to nonlinear processes promoted by intense ionizing radiation ($>10^{15}$ PW/cm^2), while advances in the technology of table-top HHG sources of femtosecond and sub-femtosecond XUV pulses have opened the way to observe the dynamics in the attosecond time scale,[10] a whole new branch of science devoted to the study of electronic motion at its natural time scale.[11] Recently, attosecond technology has been incorporated in FEL[12−14] to generate intense XUV pulses with high spatial and temporal coherence as well as short duration, with which matter can be interrogated in the nonlinear regime in a time-resolved way.[15] Finally, HHG technology has now reached the water window (3−4 nm wavelength),[16] thus making it possible to study ultrafast correlated processes in biological samples in their natural media.

The common feature to all these light sources is their ability to ionize a molecule by absorption of just a single photon. Thus, theoretical studies devoted to understanding ultrafast phenomena induced by such energetic electromagnetic radiation must necessarily deal with the problem of describing the ionization continuum. This also applies to ultrafast

dynamics induced by IR or visible pulses in which the probing step leads to ionization of the system.[17−20] Although description of the ionization continuum is rather straightforward for atomic systems, for which a large number of accurate computational tools are available,[21−25] this is not the case for molecules, for which the number of available codes is much scarcer and often limited to study ionization under significant restrictions, e.g., by assuming a single active electron (SAE) or a mean-field approximation.[26−28] However, electron correlation, a hallmark of electronic motion in bound atomic and molecular systems,[29] plays an even more prominent role when absorption of XUV and X-ray light leads to emission of photo-electrons.[24,25,30] In ionization, correlation gives rise to salient features such as Auger resonances,[31−33] associated with the formation of transiently bound, often multiply excited configurations,[34,35] whose decay is due to the coupling between different ionization channels (configuration interaction in the continuum),[36] and satellite peaks associated with orbital relaxation[37−39] and to the failure of the SAE approximation.[40,41]

Multiply excited autoionizing states, shape resonances, and collective excitations play a fundamental role in the chemistry of the interstellar medium, in the highest layer of the earth atmosphere,[42] as well as for most of the processes leading to radiation damage.[43]

Nowadays most of these ultrashort light sources can be combined with sophisticated detection techniques such as cold-

target recoil-ion mass spectrometry (COLTRIMS),[44] velocity-map imaging (VMI),[45] time-of-flight photoelectron spectrometry,[46] and high-resolution XUV spectrometry,[47] allowing for the study of photoelectron emission from atoms, molecules, and surfaces with a level of detail that would have been unthinkable only 2 decades ago. In addition to FELs and HHG generated pulses, third-generation synchrotron facilities[48−51] allow one to measure the ionization spectrum of atoms and molecules in stationary conditions with much higher resolution than before, across a wide energy range. This can also be done in association with synchronized laser pulses.[52]

It is therefore clear that theoretical efforts aimed at improving the description of ionization processes in molecules are necessary and timely to provide the support that these sophisticated experiments require. Current quantum chemistry multiconfigurational methods have nowadays reached a considerable level of sophistication in the treatment of ground and electronically *bound* excited states[53] and are able to account for electron correlation with a great level of accuracy. The variational principle is at the heart of conventional multireference calculations; however, it cannot be applied as such to the calculation of states embedded in the ionization continuum. For this reason, systematic inclusion of correlation in the ab initio description of autoionizing and scattering states in polyelectronic molecules remains a challenge. A common approach used by several authors[27,28,51,54,55] to describe the electronic continuum in molecules makes use of the static-exchange approximation (SEA),[56,57] in which the coupling between continuum states associated with different parent ions is neglected. SEA meets the minimal requirements for the treatment of the continuum, and hence it is often used as the starting point of more sophisticated treatments based on the close-coupling (CC) approximation,[58] where interchannel coupling is included. In this sense, SEA can be regarded as the equivalent for ionization of what Hartree−Fock is for the description of bound states. SEA is adequate for describing primary photoemission from valence shells or core orbitals in which the photoelectron emerges with energies of the order of ∼10 eV or more, since in these conditions the SAE picture still holds. However, SEA is not appropriate for describing ionization processes in which more than one electron participates, e.g., autoionization arising from multiply excited states, ionization with simultaneous excitation of one or more of the remaining electrons (shake ups), and so on.

Another important requirement for the description of the electronic continuum is to disentangle, across a continuous range of energies, the asymptotic distribution of the ejected electron associated with any given molecular parent ion. This can be done by *augmenting* the parent-ion states with electrons distributed in a large set of orbitals capable of reproducing the periodic oscillations characteristic of asymptotically free states. The primitive Gaussian functions normally used in QCPs rapidly exhibit numerical linear dependencies that prevent the description of more than a few radial oscillations, and hence they are not well suited to describe a free electron except for the smallest energies and in a short radial region. This limitation can be partially circumvented by going beyond the usual Gaussian type orbitals (GTOs) by using polynomial spherical GTOs,[59,60] but the continuum wave function quality still worsens when the photon energy increases and not only the outermost valence shells are involved in the photo-ionization. The radial basis suitable for this task, such as B-splines[61,62] and finite-element discrete-variable-representation

functions (FE-DVR),[63] have been employed in ad hoc codes for the electronic continuum of small systems,[34,61,64−67] mainly for diatomic molecules. These codes, however, are not easy to extend to more complicated molecules, and their treatment of short-range electronic correlation is still rudimentary if compared with standard QCPs.

To overcome the above limitations, we have developed an approach that matches the capability of state-of-the-art techniques for the calculation of correlated excited states, provided by widely available packages such as MOLCAS[68] and MOLPRO,[69] with well-established techniques for the description of the electronic continuum. We do so by using a hybrid Gaussian-B-spline basis (GABS).[70] There are other approaches based on a similar philosophy, in which a short-range part represented by GTOs is complemented with other functions more appropriate for the scattering description, such as finite-element (FE) representation of the radial coordinate,[71,72] discrete variable representation (DVR)[73−75] and plane waves.[30] Other efforts have been made within the framework of density functional theory (DFT), using for instance a multicenter expansion in B-splines.[76] Despite the existence of all these models, ours has its own advantages. Increasing the number of electrons for a fixed number of scattering channels does not make the computational cost of the full dimensional problem significantly higher. This means that the effort made to compute the helium atom would be similar to that needed to compute the water molecule for instance. Although this points to the fact that the computation of very small systems would not be very efficient, our real target, small- and medium-size molecules, would be easily achievable without serious penalties. Another benefit of our implementation is the capability to obtain from a multichannel scattering problem either time-independent observables, e.g., resonance energies and widths, or time-dependent ones, expanding for the latter the wave function in the box of eigenstates, a very convenient way to carry out the time propagation and to extract observables from it. An additional advantage is that resonances, such as doubly excited states, arise naturally from the close-coupling expansion without the need of an ad hoc inclusion, if one of them plays a key role in the dynamics. Our model can also support core holes, which will be the object of future studies.

To illustrate the viability of our approach, hereafter called XCHEM for short, we report results for the multichannel ionization of the helium atom and of the hydrogen molecule that are in excellent agreement with existing accurate benchmarks. These findings, together with the flexibility of QCPs, make this approach a good candidate for the theoretical study of the ionization of polyelectronic systems.

This work is organized as follows. Section 2 presents the theoretical background, with emphasis in our merging of scattering methods with quantum chemistry approaches, and section 3 describes the computational implementation of the new method. Results for the He and H_2 benchmark systems are given and discussed in section 4. The work finishes with some conclusions and future perspectives in section 5. Atomic units are used throughout unless otherwise stated.

2. THEORY

The single photoionization of an atomic or molecular species A by means of the absorption of one photon γ,

$$A_i + \gamma \rightarrow A_a^+ + e_{k\sigma}^- \tag{1}$$

converts the initial state $|i\rangle$ of the N-electron target to one of the energetically accessible states of the parent ion $|a\rangle$ of the (N − 1)-electron parent ion, $E_a - E_i \leq \hbar\omega_\gamma$, and liberates a photoelectron with asymptotic linear momentum $\vec{k}$ and spin projection σ. This process, therefore, involves the transition from a bound to a scattering state of the N-electron system. This latter circumstance remains true irrespective of whether the single-ionization event involves the exchange of one or several photons, possibly with different frequencies, or of whether these photons come in the form of pulses rather than in stationary conditions. Although more complex fragmentation processes, such as multiple ionization and dissociative ionization, may follow valence and inner-valence ionization of atomic and molecular species with XUV light, single ionization with (or without) electronic excitation normally dominates. Furthermore, multiple ionization processes tend to take place through a sequence of single-ionization steps when this mechanism is permitted. Therefore, single ionization can describe a broad range of phenomena. In the present work we will limit our attention to this process.

The interaction between matter and radiation is mediated by a one-body operator. To a first approximation, therefore, photoionization amplitudes can be estimated already at the SAE level. In polyelectronic targets, the interaction of the photoelectron originating from a given orbital and the other electrons in the system can be described in terms of an effective potential,[77,78] or within the Hartree,[79] Hartree−Fock,[25,80−83] or DFT approximations.[28,51,76,84] These approaches normally yield accurate photoelectron distributions at high photoelectron energies but fail to reproduce experiments at energies a few electronvolts above the ionization thresholds, where exchange and correlation effects are important.[84,85] It has been recently shown that antisymmetry needs to be taken explicitly into account to obtain qualitatively reliable results.[71] Shape resonances are also normally not well reproduced, and SAE approaches, of course, cannot account for processes associated with interchannel coupling, such as inelastic scattering and autoionizing states, particularly when the latter are populated through multiple excitations from the ground state.

The first few correlated bound electronic states of atoms and molecules, and the radiative transitions between them, can be computed quite accurately with existing QCPs. Correlated states in the electronic continuum, on the other hand, are much more challenging to obtain for three reasons. First, as mentioned above, they require the representation of oscillatory electronic wave functions up to large distances, which is challenging for the Gaussian basis sets used in QCPs. Second, the calculation of bound and scattering states requires different algorithms. For bound states, the energy is an unknown quantity that is determined through diagonalization, and degeneracy is an issue only for selected subsets of the configuration space. For ionization states, on the other hand, energy is given and, as a rule, each level is multiply or, possibly, infinitely degenerate. Simply restricting the Hamiltonian to a finite basis and diagonalizing it, therefore, is not an option. Third, the scattering states required to reproduce given experimental conditions must fulfill well-defined asymptotic boundary conditions.

A common procedure to build a complete set of scattering states at a given energy E is the CC approach. In CC, the configuration space is expressed in terms of the linear combination of antisymmetrized products of bound states of the parent ion A^+ and states of the asymptotically free electron

with a well-defined angular momentum. Indeed, when separated by large distances, the parent ion and the electron do not interact and these states are therefore sufficient to enumerate all the possible initial or final configurations of the system. When the parent ion and the electron are spatially close, they can exchange energy, angular momentum, and spin in an interaction that can be represented as a collision,

$$A_a^+ + e_{\vec{k}\sigma}^- \rightarrow A_b^+ + e_{\vec{k}'\sigma'}^- \tag{2}$$
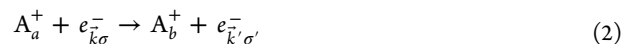
The following sections illustrate how to set up the equations that define single-ionization scattering states for polyelectronic targets, and how these can be solved numerically by making use of QCPs.

2.1. Close-Coupling Method. To describe a single-ionization scattering state, it is convenient to distinguish between two radial ranges: a short-range, $r_i < R_0$, where all N_e electrons are within a fixed radius R_0 from the conventional center of mass, and a long-range, $r_{N_e} > R_0$, where one and only one electron (e.g., the N_eth) is located beyond R_0; that is, $r_{i<N_e} < R_0$. If the boundary value R_0 is large enough, the eigenstates of the parent ion are negligible whenever $r_i > R_0$. As a result, the complete single-ionization wave function in the second region is well-represented by the CC ansatz

$$r_{N_e} > R_0,$$

$$\Psi_{\alpha E}^-(\mathbf{x}_1, ..., \mathbf{x}_{N_e}) = \frac{1}{N_e} \sum_\beta N_{\beta E} \Upsilon_\beta(\mathbf{x}_1, ..., \mathbf{x}_{N_e-1}; \hat{r}_{N_e}, \zeta_{N_e}) \frac{u_{\beta,\alpha E}^-(r_{N_e})}{r_{N_e}} \tag{3}$$

where $\mathbf{x}_i$ denotes the position and spin coordinates of electron i, $\hat{r}_{N_e}$ are the angular coordinates of electron N_e, ζ_{N_e} is the spin component of electron N_e, Υ_α is a spin-coupled channel function (see below), $N_{\beta E}$ is a normalization factor that ensures the correct asymptotic behavior, and $u_{\beta,\alpha E}^-(r)$ is the radial function that describes the continuum electron, which is asymptotically given by

$$u_{\beta,\alpha E}^-(r) = \delta_{\alpha\beta} \sqrt{\frac{2}{\pi k_\alpha}} e^{i\Theta_\alpha(r)} - \sqrt{\frac{2}{\pi k_\beta}} e^{-i\Theta_\beta(r)} \mathbb{S}_{\beta\alpha}^* \tag{4}$$

with

$$\Theta_\alpha(r) = k_\alpha r + \frac{Z}{k_\alpha} \ln 2k_\alpha r - l_\alpha \pi/2 + \sigma_{l_\alpha}(k_\alpha) \tag{5}$$

where $\mathbb{S}_{\alpha\beta}$ is the *on-shell* scattering matrix,[86,87] Z the parent-ion charge, k_α the absolute value of the momentum of the continuum electron in the α channel, and σ_{l_α} its Coulomb phase. Thus, the scattering wave function $\Psi_{\alpha E}^-$ behaves asymptotically as a combination of incoming spherical waves for all open channels (α, β, and γ in Figure 1) and an outgoing spherical wave in channel α corresponding to an outgoing flux of 1.

In the present work, the spin-coupled channel function Υ_α is obtained when the antisymmetrized parent-ion function Φ_a is coupled to the N_eth electron spin wave function χ, while its angular part, given by a spherical harmonic Y_{lm}, is factorized:
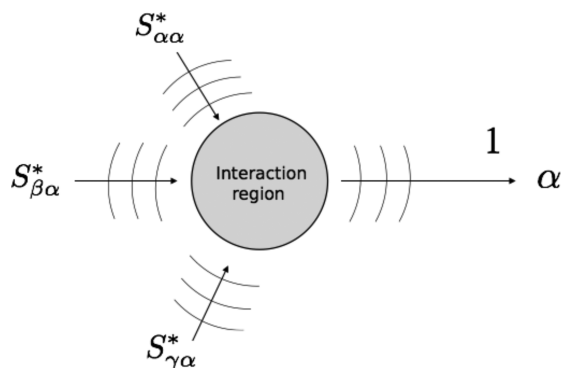
Figure 1. Sketch of the incoming boundary conditions that must fulfill the scattering wave function $\Psi_{\alpha E}^{-}$ (see text for notations).

$$\Upsilon_\alpha(\mathbf{x}_1, ..., \mathbf{x}_{N_e-1}; \hat{r}_{N_e}, \zeta_{N_e}) \tag{6}$$
$$= {}^{2S+1}[\Phi_a(\mathbf{x}_1, ..., \mathbf{x}_{N_e-1}) \otimes {}^2\chi(\zeta_{N_e})]_\Sigma \, Y_{lm}(\hat{r}_{N_e})$$
$$= \sum_{\Sigma_a \sigma} C^{S\Sigma}_{S_a\Sigma_a,1/2\sigma} \, {}^{2S_a+1}\Phi_{a,\Sigma_a} {}^2\chi_\sigma(\zeta_{N_e}) \, Y_{lm}(\hat{r}_{N_e}) \tag{7}$$

where S is the total spin of the system, Σ is its z projection, S_a and Σ_a are the corresponding values for the parent ion, σ is the z component of the electron spin, and $C^{S\Sigma}_{S_a\Sigma_a,1/2\sigma}$ is a Clebsh–Gordan coefficient. For the sake of clarity, the spin multiplicity of both the parent-ion and continuum-electron components, $2S_a + 1$ and 2, respectively, have been indicated as prefixes of the corresponding wave functions. The channel index α corresponds to the set of indexes (S,Σ,a,l,m), while the parent-ion index a defines entirely the state of the parent ion, except for its total spin projection. We will be mostly interested in spin-free Hamiltonians. Therefore, the total spin S and spin-projection Σ will be constant parameters across the whole scattering calculation.

Due to the natural asymptotic separation between a finite number (or a denumerable set) of channel functions $\Upsilon_\alpha(\mathbf{x}_1,...,\mathbf{x}_{N_e-1};\hat{r}_{N_e},\zeta_{N_e})$ and the radial wave function of an electron in the continuum, in a scattering perspective we describe the complete function as a linear combination of "extended" channel functions $\overline{\Upsilon}_{\alpha i}$ and of localized short-range N_e-electron states $\aleph_i$:

$$\Psi_{\alpha E}^{-} = \sum_i \aleph_i c_{i,\alpha E} + \sum_\beta \sum_i \tilde{\Upsilon}_{\beta i} c_{\beta i,\alpha E}. \tag{8}$$

The extended channel functions $\overline{\Upsilon}_{\alpha i}$ are defined as

$$\overline{\Upsilon}_{\alpha i} = N_{\alpha i} \hat{\mathcal{A}} \Upsilon_\alpha(\mathbf{x}_1, ..., \mathbf{x}_{N_e-1}; \hat{r}_{N_e}, \zeta_{N_e}) \, \varphi_i(r_{N_e}) \tag{9}$$

where $\{\varphi_i\}$ is a set of radial functions suitable to describe the continuum and $\hat{\mathcal{A}}$ is the antisymmetrizer

$$\hat{\mathcal{A}} = \frac{1}{N!} \sum_{\mathcal{P} \in \mathcal{S}_{N_e}} (-1)^p \mathcal{P}, \quad p = \text{parity of } \mathcal{P} \tag{10}$$

with $\mathcal{P}$ the standard permutation operator that belongs to the space of N_e-particle permutations, $\mathcal{S}_{N_e}$. The channel functions Υ_α are assumed to be already totally antisymmetric with respect to the permutation of the first $N_e - 1$ parent-ion electrons

$$\forall \, \mathcal{P} \in \mathcal{S}_{N_e-1},$$
$$\mathcal{P}\Upsilon_\alpha(\mathbf{x}_1, ..., \mathbf{x}_{N_e-1}; \hat{r}_{N_e}, \zeta_{N_e})$$
$$= (-1)^p \Upsilon_\alpha(\mathbf{x}_1, ..., \mathbf{x}_{N_e-1}; \hat{r}_{N_e}, \zeta_{N_e}) \tag{11}$$

The antisymmetrizer for N_e particles $\hat{\mathcal{A}}^{(N_e)}$ can be written in terms of that for $N_e - 1$ particles, $\hat{\mathcal{A}}^{(N_e-1)}$:

$$\hat{\mathcal{A}}^{(N_e)} = \frac{1}{N_e}\left(1 - \sum_{i=1}^{N_e-1} \mathcal{P}_{iN_e}\right)\hat{\mathcal{A}}^{(N_e-1)} \tag{12}$$

where $\mathcal{P}_{iN_e}$ denotes the permutation operator between particles i and N_e. Therefore, the extended channel functions can also be written as

$$\overline{\Upsilon}_{\alpha i} = \frac{N_{\alpha i}}{N_e}\left(1 - \sum_{i=1}^{N_e-1} \mathcal{P}_{iN_e}\right) \Upsilon_\alpha(\mathbf{x}_1, ..., \mathbf{x}_{N_e-1}; \hat{r}_{N_e}, \zeta_{N_e}) \, \varphi_i(r_{N_e}) \tag{13}$$

2.2. Equivalence between Extended Channel Functions and Augmented States. QCPs can provide an accurate description of the parent-ion states. To account for the additional continuum electron, these states must be supplemented with additional one-electron functions, which can be done in practice by using the so-called *augmented states*, defined as

$$\overline{\Upsilon}_{\alpha i}^{aug} = \hat{P}^{S\Sigma} \hat{a}_{il_a m_a \sigma}^\dagger \Phi_{a,\Sigma_a} \tag{14}$$

for an orbital with well-defined l_α and m_α quantum numbers, where $P^{S\Sigma}$ is the *projector* on the functions with total spin S and spin projection Σ, $\hat{a}_{ilm\sigma}^\dagger$ is the creation operator of an electron in the spin–orbital $\phi_i(\mathbf{x}) = \phi_i(r) \, Y_{lm}(\hat{r}) \, {}^2\chi_\sigma(\zeta)$, and Φ_{a,Σ_a} is a parent-ion state with well-defined total spin projection Σ_a. For simplicity in the notation, the l, m, and σ quantum numbers are implicit in the i index used to denote a particular spin–orbital $\phi_i(\mathbf{x})$. The creation operator is defined on the space of spin–orbital occupation-number vectors as

$$\hat{a}_i^\dagger |n_1, n_2, ..., \overset{i}{0}, ...\rangle = (-1)^{\sum_{j=1}^{i-1} n_i}|n_1, n_2, ..., \overset{i}{1}, ...\rangle \tag{15}$$

$$\hat{a}_i^\dagger |n_1, n_2, ..., \overset{i}{1}, ...\rangle = 0 \tag{16}$$

Furthermore, the spin–orbital occupation-number vectors are identified with Slater determinants as

$$\langle \mathbf{x}_1, \mathbf{x}_2 ..., \mathbf{x}_{N_e}|n_1, n_2, ...\rangle = \sqrt{N_e!}\,\hat{\mathcal{A}} \prod_{i=1}^{\infty} \phi_i^{n_i}(\mathbf{x}_{N_i}),$$
$$N_i = \sum_{j=1}^{i} n_j \tag{17}$$

What is the exact relation between the augmented states and the extended channel functions introduced in the preceding subsection? In the close-coupling formalism, the antisymmetrization of the product of an $(N_e - 1)$-electron determinant $|\phi_{k_1}...\phi_{k_{N_e-1}}|$ times a given spin orbital ϕ_i is

$$\hat{\mathcal{A}}|\phi_{k_1} ... \phi_{k_{N_e-1}}|\phi_i = \frac{1}{\sqrt{N_e}}|\phi_{k_1} ... \phi_{k_{N_e-1}}\phi_i| \tag{18}$$

Whenever the appended spin−orbital follows all the occupied spin−orbitals in the determinant (as it is always the case when augmenting a parent ion with a virtual orbital), the following relation holds:

$$\hat{\mathcal{A}}\Phi_a\phi_i = \frac{1}{\sqrt{N_e}}(-1)^{N_e-1}\hat{a}_i^\dagger\Phi_a \tag{19}$$

Using the definition of the augmented states and of the extended channel functions, it is therefore easy to derive the following relation:

$$\overline{\Upsilon}_{\alpha i}^{aug} = (-1)^{N_e-1}\frac{\sqrt{N_e}}{N_{\alpha i}}C_{S_a\Sigma_a 1/2\sigma}^{S\Sigma}\overline{\Upsilon}_{\alpha i} \tag{20}$$

3. IMPLEMENTATION

3.1. Parent Ions. The parent-ion wave functions are calculated using multiconfigurational methods, i.e., the wave function of every parent ion, a vector in the configuration interaction (CI) picture, is represented by a linear combination of configuration state functions (CSFs) as

$$|\Phi_a(\mathbf{x})\rangle = \sum_i c_{ia}|^{2S_a+1}_q\Xi_i(\mathbf{x})\rangle \tag{21}$$

where $|^{2S_a+1}_q\Xi_i(\mathbf{x})\rangle$ represents an $(N_e - 1)$-electron CSF with multiplicty $2S_a + 1$ and symmetry q. These CSFs can be related to Slater determinants using the graphical unitary group approach (GUGA),[88] avoiding the possibility of spin contamination, so that the eigenfunction a can be converted into combinations of Slater determinants (D_i), key pieces in second quantization theory,[89] as

$$|\Phi_a(\mathbf{x})\rangle = \sum_i c'_{ia}|D_i(\mathbf{x})\rangle \tag{22}$$

where the orbitals included in the Slater determinants are constructed as a linear combination of localized Gaussian functions

$$\phi_i^L(\mathbf{x}_1) = \sum_j R_{ji}^L G_j^L(\mathbf{x}_1) \tag{23}$$

R_{ji}^L being the expansion coefficient for the orbital i in the localized Gaussian basis function G_j^L. It is important to remember that Gaussian basis functions are centered on the different nuclei of the molecule, which requires the evaluation of polycentric integrals to calculate the properties of the system. For reasons that will become apparent later, in the latter equation we have included a superscript L to explicitly indicate that all these functions are localized.

The optimization of the orbitals and CI vectors can be done using standard quantum chemistry methods. Specifically, we use the complete active space self-consistent method (CASSCF) where the orbitals are divided into inactive, active, and virtual subspaces. The inactive and virtual orbitals are doubly occupied and empty, respectively. The active orbitals define the so-called active space and the CI vector is constructed in the CSF basis considering all possible configurations for the electrons in this reduced set of orbitals, i.e., a full CI calculation inside the active space. To allow for the description of different parent ions with the same set of orbitals, parent-ion states are obtained by using the state-average formalism, SA-CASSCF.[90] The orbitals are calculated, imposing symmetry constraints, using the QCP MOLPRO,[69] which

allows one to average states of different symmetries. In this way, all the states are represented in the same set of orbitals irrespective of the symmetry group to which they belong, and, consequently, the size of the active space can be substantially enlarged by using symmetry considerations. Furthermore, as symmetry is well-defined in both the CI vector and the orbital representation, one can also exploit symmetry properties in the augmentation procedure described in section 3.3. The set of orbitals resulting from MOLPRO is then transformed to make it compatible with the MOLCAS[91] code, and the CI vector of eq 21 is recalculated preserving the symmetry constraints. The required matrix elements, Hamiltonian and multipoles up to fifth order between the parent ions, are calculated by using the RASSI module of MOLCAS. Finally, in order to further manipulate the electronic wave function, the CI vector is transformed into a linear combination of Slater determinants using the GUGA table provided by MOLCAS, thus leading to parent-ion wave functions in the form given by eq 22.

3.2. GABS Hybrid Basis. The localized functions used to expand the short-range domain are supplemented by a monocentric GABS basis,[70] placed at the molecular center of mass. This basis has recently been introduced by Marante et al.[70] to investigate photoionization of the hydrogen atom. In brief, the GABS basis comprises a set of Gaussian functions and a set of B-splines whose support starts from a given radius R_0 (see Figure 2). The Gaussian functions are numerically
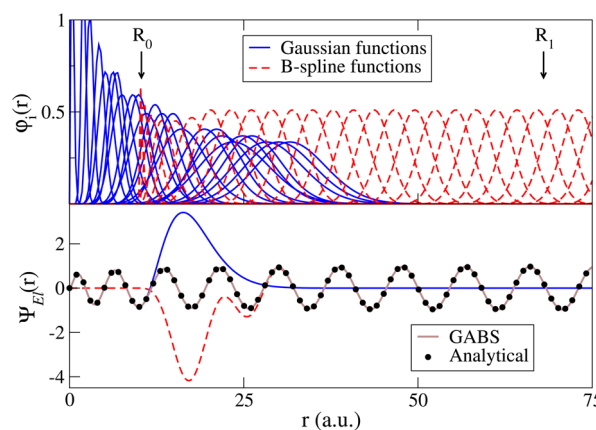

Figure 2. Top panel: Plot of the radial part of some Gaussian (solid lines) and B-spline (dashed lines) functions, representatives of the monocentric GABS basis set as a function of the distance from the origin. The first B-spline node is located at $R_0 = 10$ au. The basis defines three characteristic regions: (i) $r \in [0,R_0]$, where only Gaussian functions are present, (ii) $r \in [R_0,R_1]$, where Gaussian and B-spline functions overlap, and (iii) $r \in [R_1,R_{box}]$ where the Gaussian functions are negligible. Bottom panel: Radial part of the He$^+$ scattering state with $l = 1$ and $E = 0.2$ au, computed analytically (dots) and numerically using GABS (thick solid line). The Gaussian (solid line) and the B-spline (dashed−dotted line) components of the numerical function are also shown.

negligible beyond a distance R_1 higher than R_0. Due to this, functions expressed in terms of the GABS basis are exclusively represented by Gaussian functions for $r < R_0$, by a combination of Gaussian functions and B-splines in the intermediate region where the former are nonvanishing, and only by B-splines thereafter.

The set of Gaussian functions included in the GABS basis is in general more flexible than those included by default in
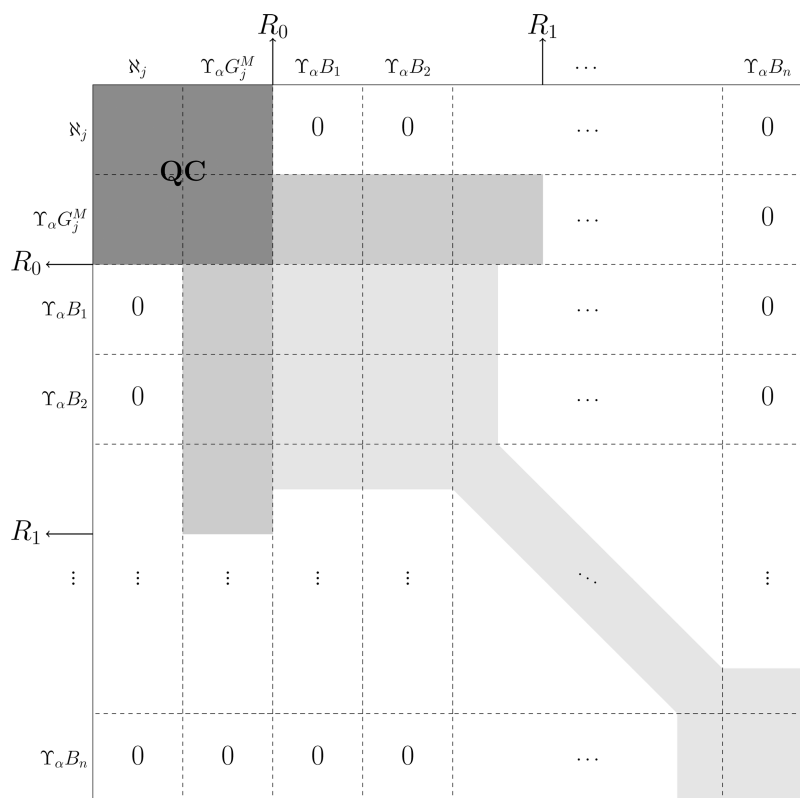
Figure 3. Matrix structure of the Hamiltonian operator. See text for notations. Shaded areas represent matrix blocks containing nonzero matrix elements. The QC block is obtained from the QCPs. The remaining matrix elements are evaluated by using the equations given in the Appendix.

QCPs. For a given angular momentum l and projection m, they are defined as

$$G_{iK}^{lm}(\mathbf{x}) = N_{il} r^K e^{-\alpha_i r^2} X_{lm}(\hat{r}) \quad (24)$$

where $K = l, l + 2, l + 4, ..., K_{max}$, and N_{li} is a normalization factor. The X_{lm} functions are the symmetry adapted spherical harmonics, also known as real spherical harmonics,[92] defined through the spherical harmonics Y_{lm} and for $m > 0$ by

$$X_{l0}^S = Y_{l0}$$

$$X_{lm}^S = \frac{1}{\sqrt{2}}((-1)^m Y_{lm} + Y_{l-m})$$

$$X_{l-m}^S = \frac{1}{i\sqrt{2}}((-1)^m Y_{lm} - Y_{l-m}) \quad (25)$$

Note that the symmetry adapted spherical harmonics defined in this equation are not the same that the ones used in the XCHEM code, i.e., $X_{lm} = (-1)^m X_{lm}^S$.

B-spline functions are a minimal-support basis for piecewise polynomials of degree $k - 1$ and defined in a set of nodes $\{t_i\}_{i=1,2,...,n}$.[93] The support of each B-spline is compact and covers k consecutive intervals, allowing local operators to be represented by sparse matrices. This property imparts high flexibility to the basis without affecting numerical accuracy, explaining why B-splines are widely used for atomic and molecular calculations.[61,62]

In the extended channel functions (eq 9), the one-electron radial functions $\varphi_i(r)$ are represented by the GABS basis. This basis allows the parent ions to be augmented using Gaussian functions in the short range, while B-splines are responsible for describing the oscillations of the continuum-electron wave

function in the field of the parent ion. The upper panel of Figure 2 shows a typical GABS basis set.

As an illustration of the performance of the GABS basis, we compare in Figure 2 (lower panel) the radial part of the exact He^+ continuum wave function for an electron with energy $E = 0.2$ au above the ionization threshold with that obtained by using the GABS basis. The two curves are indistinguishable to the naked eye. The presence of B-spline functions in the long and intermediate ranges ($r > R_0$) gives more flexibility to the Gaussian functions in the short range. This is the reason for the large deviation of the Gaussian contribution to the continuum wave function in the intermediate radial range, which is largely compensated by the B-spline contribution. More details about the GABS basis can be found in ref 70.

It is worth emphasizing that, at variance with existing all-B-spline methods,[61,62] in which B-splines are used for both the inner and the outer regions, e.g., by fitting the electronic density obtained with ordinary Gaussian functions in the inner region,[76,85] in our approach B-splines are used to supplement Gaussian basis sets provided by quantum chemistry packages and subsequently augmented with the monocentric Gaussian functions included in the GABS basis. The procedure adopted to perform the augmentation is described in the following subsection.

3.3. Augmentation. In order to calculate the augmented states, the virtual orbitals of the parent ion (defined as linear combinations of the localized Gaussian functions centered at the atomic positions) are removed, while the auxiliary set of Gaussian functions belonging to the GABS basis and located on the center of mass is added; i.e., we follow a strategy similar to that usually employed to describe Rydberg states.[94] As explained above, these Gaussian functions will help us to

reproduce the electronic continuum close to the nuclear region by providing a set of mainly monocentric orbitals that connect the localized ones at short distances with B-spline functions at long distances.

The monocentric orbitals, ϕ^M, are constructed by removing linear dependencies and orthogonalizing them to the localized orbitals ϕ^L:

$$\phi_i^M(\mathbf{x}_1) = \sum_j R_{ji}^M G_j^M(\mathbf{x}_1) + \sum_j a_{ji} \phi_j^L(\mathbf{x}_1) \tag{26}$$

where R_{ji}^M are the linearly independent components of the orbital i in the monocentric Gaussian functions G_j^M and a_{ji} contains the contribution of the localized orbital j to fulfill the orthonormalization requirements. For the sake of clarity, we have dropped all indices but one in the definition of the monocentric Gaussian functions given in eq 24 and we have explicitly added the superscript M to emphasize the monocentric character of these functions.

The augmentation procedure is carried out for all chosen parent-ion states over all possible orbitals, both localized (ϕ_i^L, eq 23) and monocentric (ϕ_i^M, eq 26),

$$|\overline{\Phi}_{ai}(\mathbf{x})\rangle = a_i^\dagger |\Phi_a(\mathbf{x})\rangle \tag{27}$$

where $\overline{\Phi}_{ai}$ describes the parent ion a augmented in the orbital i. This augmentation is easy to implement when the parent ions are described in the basis of Slater determinants (see eq 22) as

$$|\overline{\Phi}_{ai}(\mathbf{x})\rangle = \sum_j c'_{ja} a_i^\dagger |D_j(\mathbf{x})\rangle \tag{28}$$

This function is then projected into a basis with a well-defined spin, using the GUGA table of the parent ion with an extra electron, to obtain the augmented state defined in eq 14:

$$|\overline{\Upsilon}_{ai}^{aug}(\mathbf{x})\rangle = \sum_k c''_{k\alpha i} |^{2S+1}\Xi_k(\mathbf{x})\rangle \tag{29}$$

where the elements $c''_{k\alpha i}$ are given by

$$c''_{k\alpha i} = \sum_j c'_{ja} \langle^{2S+1}\Xi_k(\mathbf{x})|a_i^\dagger |D_j(\mathbf{x})\rangle \tag{30}$$

and we have used the fact that $\alpha \equiv (S,\Sigma,a,l,m)$. Finally, all the properties between the different augmented parent ions, i.e., the Hamiltonian, overlap, and dipole matrices, are obtained with the RASSI module of MOLCAS.

3.4. Scattering States. From the equations provided in the CC section 2.1 and in the Appendix, the Hamiltonian (eq 51) and overlap (eq 45) operator matrices can be computed and, using these, the scattering states obtained. The block structure of the operators is shown in Figure 3. The $\aleph_j$ functions represent the N_e-electron localized states (obtained using a polycentric Gaussian expansion), the $\Upsilon_\alpha G_j^M$ ones involve the parent-ion wave functions augmented with the monocentric Gaussian set (which are related to the extended channel functions as explained in section 2.2), and the $\Upsilon_\alpha B_k$ functions represent the extended channel functions with B-splines B_k for the outer electron. In this notation, α runs over all channels included in the CC ansatz. The blocks that cross the wave functions exclusively expanded in terms of Gaussian functions are computed with the QCPs. To compute the other matrix elements, the equations given in the Appendix have been used. In the present work, we neglect the overlap between polycentric Gaussian functions and B-splines. This is a good approximation since the former are strongly localized by

construction and the latter start at several Bohr radii from the molecular center. Beyond a certain radius R_1, even the overlap between the fast-decreasing monocentric Gaussian functions and the B-splines becomes negligible, and then, from that distance on, these blocks will be zero as well. This last feature together with the fact that B-spline functions have a compact support lead to sparse matrices, whose structure can be exploited when operating with them. The zero blocks in Figure 3 are represented by a white background.

To compute the scattering solution $\Psi_{\alpha E}^-$, we require $(\hat{H} - E)\Psi_{\alpha E}^-$ to vanish when projected onto the N basis functions that are zero at the box boundary (i.e., the farthest grid point used in the definition of the B-spline basis). If the CC expansion includes M channels Υ_β that are open at the energy E, the corresponding components of $\Psi_{\alpha E}^-$ generally do not all vanish at the box boundary and they must therefore include the last B-spline in the box. These two requirements lead to a $N \times (N + M)$ homogeneous system of linear equations which has M nontrivial solutions:

$$(\mathbf{H} - E\mathbf{S}) \cdot \mathbf{\Psi} = \mathbf{0} \tag{31}$$

To solve eq 31, we require the left-hand matrices to contain linearly independent rows and columns. Let us call $\mathbf{O_p}$ the matrix representation of an operator O in the same basis as that used to express the Hamiltonian matrix in Figure 3. In general, the operator blocks coming from QCPs exhibit linear dependencies. Similarly, the blocks in which the bras correspond to a parent ion augmented with monocentric Gaussian functions and the kets correspond to a parent ion coupled with B-splines or vice versa can also have linear dependencies, because several of the Gaussian functions can be represented by linear combinations of B-splines. We will call the ensemble of these blocks $\mathbf{O_p}'$, whose equivalent is the submatrix limited by R_1 in Figure 3. In other words, $\mathbf{O_p}'$ contains the QC matrix elements and the rows and columns in which there is a non-negligible overlap between monocentric Gaussian and B-spline functions. In contrast, the blocks in which bras and kets involve only B-splines are linearly independent due to the effective completeness of this basis.[95] To eliminate the linear dependencies, $\mathbf{O_p}$ is converted to a conditioned version $\tilde{\mathbf{O}}_\mathbf{p}$ by means of the transformation

$$\tilde{\mathbf{O}}_\mathbf{p} = \mathbf{P}_{con}^T \mathbf{O_p} \mathbf{P}_{con} \tag{32}$$

The conditioning matrix $\mathbf{P}_{con}$ is given by

$$\mathbf{P}_{con} = \left[\begin{array}{c|c} \tilde{\mathbf{V}}\tilde{\mathbf{\Lambda}}^{-\frac{1}{2}} & \mathbf{0} \\ \hline \mathbf{0} & \mathbf{1} \end{array} \right] \tag{33}$$

where $\tilde{\mathbf{V}}$ and $\tilde{\mathbf{\Lambda}}$ are, respectively, the eigenvector and eigenvalue matrices resulting from the diagonalization of the overlap submatrix $\mathbf{S}'$ (equivalent to $\mathbf{O_p}'$) after removal of those eigenvectors whose associated eigenvalues are lower than some threshold (typically 10^{-8}). Therefore, $\mathbf{P}_{con}$ only transforms the square block $\mathbf{O_p}'$.

After conditioning the overlap and the Hamiltonian matrices, the system of linear eqs 31 can be rewritten as

$$(\tilde{\mathbf{H}} - E\tilde{\mathbf{S}}) \cdot \tilde{\mathbf{\Psi}} = \mathbf{0} \tag{34}$$

where the new solutions $\tilde{\mathbf{\Psi}}$ are related to the original ones by $\mathbf{\Psi} = \mathbf{P}_{con}\tilde{\mathbf{\Psi}}$. The system of linear eqs 34, now free from linear dependencies, has M independent solutions. To find them, we use standard linear-algebra routines that factorizes the $\tilde{\mathbf{H}} - E\tilde{\mathbf{S}}$

matrix in the product of a lower triangular $N \times (N + M)$ matrix $\mathbf{L}$ and an upper triangular $(N + M) \times (N + M)$ matrix $\mathbf{U}$, which has M zeros along the diagonal, $\tilde{\mathbf{H}} - E\tilde{\mathbf{S}} = \mathbf{L}\mathbf{U}$. Therefore, the solutions of eq 34 are just the solutions of

$$
\mathbf{U} \cdot \tilde{\boldsymbol{\Psi}} =
\begin{bmatrix}
u_{11} & u_{12} & \cdots & u_{1N} & & \cdots & & u_{1n} \\
0 & u_{22} & \cdots & u_{2N} & & \cdots & & u_{2n} \\
\vdots & \vdots & \ddots & & & \cdots & & \vdots \\
0 & 0 & \cdots & u_{NN} & & \cdots & & u_{Nn} \\
0 & 0 & 0 & \cdots & 0 & u_{(N+1)(N+2)} & \cdots & u_{(N+1)n} \\
0 & 0 & 0 & 0 & & \cdots & 0 & \cdots & u_{(N+2)n} \\
\vdots & \vdots & \vdots & \vdots & \vdots & \vdots & & \ddots & \vdots \\
0 & 0 & 0 & 0 & 0 & 0 & & \cdots & 0
\end{bmatrix}
$$

$$
\times
\begin{bmatrix}
\tilde{\Psi}_{11} & \tilde{\Psi}_{12} & \cdots & \tilde{\Psi}_{1M} \\
\tilde{\Psi}_{21} & \tilde{\Psi}_{22} & \cdots & \tilde{\Psi}_{2M} \\
\vdots & \vdots & \ddots & \vdots \\
\tilde{\Psi}_{N1} & \tilde{\Psi}_{N2} & \cdots & \tilde{\Psi}_{NM} \\
-1 & 0 & \cdots & 0 \\
0 & -1 & \cdots & 0 \\
\vdots & \vdots & \ddots & \vdots \\
0 & 0 & \cdots & -1
\end{bmatrix}
= \mathbf{0}
\tag{35}
$$

i.e., they constitute the right null space of $\mathbf{U}$, which can easily be determined by back-substitution.

The radial monoelectronic function coupled to the parent ions in the scattering solution (see eqs 8 and 9) appears as a linear combination of orbitals containing both Gaussian and B-spline functions

$$
\phi_{\beta\alpha}(r) = \sum_i N_{\beta i} \varphi_i(r) c_{\beta i,\alpha E}
\tag{36}
$$

and is asymptotically fitted to a combination of regular, $F(r)$, and irregular, $G(r)$, Coulomb functions[96]

$$
\phi_{\beta\alpha}(r) = a_{\beta\alpha} F_\beta(r) + b_{\beta\alpha} G_\beta
\tag{37}
$$

From this fit, we can compute the scattering matrix $\mathbb{S}(E, E')$ for the elastic collision, $\mathbb{S}(E)\,\delta(E - E') = \langle \Psi_E^- | \Psi_{E'}^+ \rangle$, as

$$
\mathbb{S} = \frac{\mathbf{A} + i\mathbf{B}}{\mathbf{A} - i\mathbf{B}}
\tag{38}
$$

where $A_{\beta\alpha} = \sqrt{\frac{\pi k_\beta}{2}}\, a_{\beta\alpha}$ and $B_{\beta\alpha} = \sqrt{\frac{\pi k_\beta}{2}}\, b_{\beta\alpha}$, with k_β being the momentum relative to the threshold defined by the β-parent ion. Using these matrices, we can also obtain the correct scattering wave function with incoming boundary conditions through

$$
\Psi_{\alpha E}^- = \sum_\beta \Psi_{\beta E} (A_{\beta\alpha} + iB_{\beta\alpha})^{-1}
\tag{39}
$$

where $\Psi_{\beta E}$ are the solutions of eq 31. The eigenvalues of $\mathbb{S}$ have the form $e^{2i\theta_\alpha}$, where θ_α ($\alpha = 1, ..., M$) are the so-called phase shifts or eigenphases,[97,98] which can be used as a sensitive observable to check the accuracy of the calculation of the multichannel continuum by comparing them to independently established benchmarks. In the presence of an isolated resonance, the sum over all the eigenphases, the total phase shift $\theta_T(E)$, experiences a jump of π when the energy moves

from well below the resonance energy to well above it ($2\frac{|E - E_{\text{res}}|}{\Gamma} \gg 1$). In the presence of several resonances, their energies E_n and total widths Γ_n can be extracted by fitting the total phase shift with the function

$$
\theta_T(E) = \theta_0(E) + \sum_n \arctan\left(\frac{\Gamma_n}{2(E_n - E)}\right)
\tag{40}
$$

where $\theta_0(E)$ is a background, approximated by a low-order polynomial function of the energy.

Another observable of interest is the photoionization cross-section from the ground state (Ψ_g). To compute this quantity, we need the calculated multichannel scattering states and the ground state obtained, for instance, from the diagonalization of the Hamiltonian in a box. In velocity gauge, the photoionization cross-section is given by

$$
\sigma_{\alpha E} = \frac{4\pi^2}{c(E - E_g)} |\langle \Psi_{\alpha E}^- | \hat{\varepsilon} \cdot \mathbf{P} | \Psi_g \rangle|^2
\tag{41}
$$

where c is the speed of light, E_g is the ground state energy, $\hat{\varepsilon}$ is the polarization of the incident light, and $\mathbf{P}$ is the momentum operator.

4. PERFORMANCE OF THE XCHEM METHOD

4.1. Ionization of the Helium Atom. The helium atom is a good system to test the XCHEM method because accurate independent ab initio codes are available for it.[99]

The hydrogenic parent-ion states of He$^+$ were obtained by performing a SA-CASSCF calculation of five states, where the active space consists of one electron and five orbitals: 1s, 2s, $2p_x$, $2p_y$, and $2p_z$. For this computation we used a modified version of the aug-cc-pV6Z[100] basis set, where only the s and p expansions were considered. As mentioned in section 3.1, the orbitals are obtained with the MOLPRO package within D_{2h} symmetry (two states for symmetry A_g and one state for the symmetries B_{1u}, B_{2u}, and B_{3u}) and exported to MOLCAS. With MOLCAS we generate two different GUGA tables, CAS(1,5) for the case of the parent ions and CAS (2,7) for the case of the neutral, needed to carry out the augmentation.

For the monocentric GABS basis, B-splines of order 7 were used starting at $R_0 = 10$ au, in a box of 400 au, with a uniform grid of 0.5 au separation between consecutive nodes. The Gaussian functions in eq 24 were generated using an even-tempered set of 22 exponents, with $\alpha_1 = 0.01$, $\alpha_{22} = 28.28$, and $K_{max} = 3$.

Using this GABS basis, we defined three different CC ansatzes (3), with total multiplicity $2S + 1 = 1$ (see Table 1). The first one (CC$_1$) contains two helium parent ions, He$^+$(1s) and He$^+$(2s), while the second and the third CC ansatzes (CC$_2$ and CC$_3$) have the extra parent ion He$^+$(2p) and are intended

Table 1. CC Ansatzes Used for the Helium Atom Computations[a]

configurations	CC$_1$[b]	CC$_2$	CC$_3$
	$1s \otimes X_{lm}$	$1s \otimes X_{00}$	$1s \otimes X_{1m}$
	$2s \otimes X_{lm}$	$2s \otimes X_{00}$	$2s \otimes X_{1m}$
		$2p \otimes X_{1m}$	$2p \otimes X_{00}, X_{2m}$

[a]For each angular momentum, the projection m takes all the possible values. [b]$l = 0, 1, 2$.

to build up the channels with symmetries $^1S^e$ and $^1P^o$, respectively.

Using the CC_1 ansatz, we obtained the Hamiltonian spectrum in the box. Several of its Rydberg state energies converging to the $N = 1$ threshold (-2 au) are shown in Table 2. As a reference, an ab initio code relying exclusively on B-

Table 2. Energies (au) of Several Rydberg States Converging to the $N = 1$ Ionization Threshold of He (-2 au), Obtained by Using B-Splines Only (Reference Calculation) and the CC_1 Ansatz Given in Table 1

state	B-splines	CC_1
$1s5s$	−2.021053	−2.021047
$1s3d$	−2.019996	−2.019996
$1s4p$	−2.019821	−2.019814
$1s6s$	−2.014493	−2.014486
$1s4d$	−2.013887	−2.013879
$1s5p$	−2.013785	−2.013777
$1s7s$	−2.010582	−2.010574
$1s5d$	−2.010203	−2.010195

splines and resembling the same correlation level imposed by the CC_1 ansatz was used. This independent method yields accurate solutions for the bound and single-ionization states of the helium atom in the electrostatic approximation.[99] The agreement is very good, due to the fact that the Rydberg states' ripples, dominant in the middle and long ranges, are mainly reproduced by the B-splines, whereas the short-range part is accounted for by Gaussian functions.

Figure 4 shows the total phase shifts, $\theta(E)$ [see eq 40], for the CC_2 and CC_3 ansatzes in the vicinity of the first two $^1S^e$ and $^1P^o$ resonances below the $N = 2$ threshold (-0.5 au). In this energy region, only one channel is opened for each symmetry. The presence of the resonances is clearly recognized from the

jumps of π in the total phase shift. By fitting $\theta(E)$ to eq 40, we have extracted the corresponding energy positions and autoionization widths. The agreement with the reference calculations is very good. For the energies, the maximum absolute deviation is quite small: 0.002 au. For the widths, the error is smaller than 6%, except for the first resonance of the $^1S^e$ series, for which it is ~20%.

Figure 5 shows the eigenphases in the energy region between the $N = 2$ and $N = 3$ thresholds, where several channels are
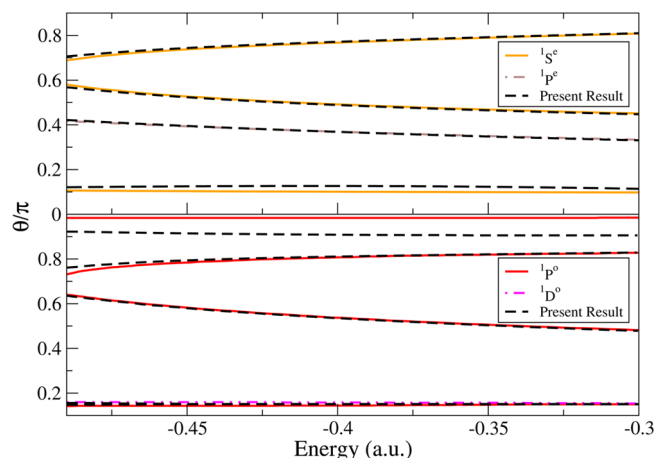

Figure 5. Multichannel scattering total phase shifts above the $N = 2$ (-0.5 au) threshold. The top panel shows the channels with even symmetry and the bottom panel those with odd symmetry.

opened for both the CC_2 and CC_3 ansatzes. This region does not feature any resonance because we are excluding all the parent ions beyond the $N = 2$ threshold from the configuration space. Once again, the calculated eigenphases computed with XCHEM compare very well with the benchmark. Only for
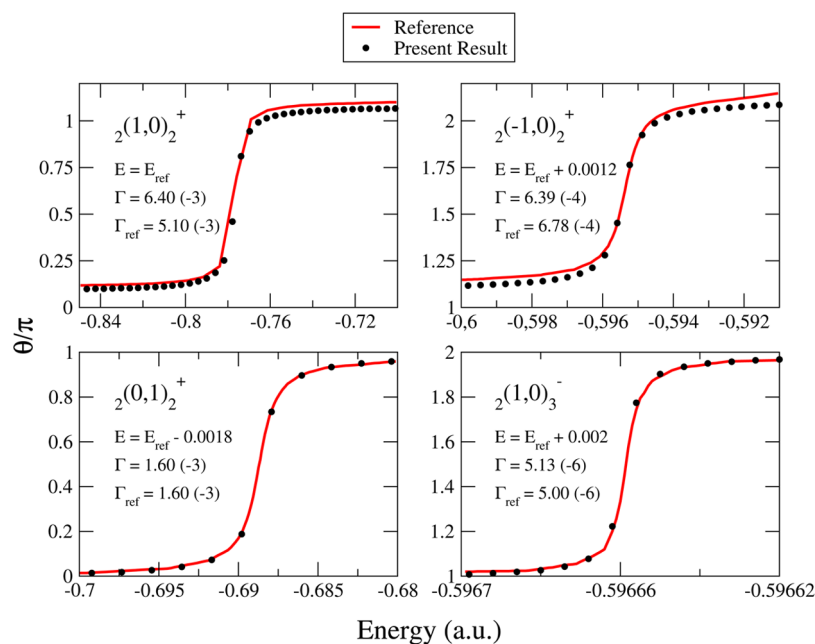

Figure 4. Total phase-shift energy dependence in units of π. The two top panels and the two bottom panels show the first two resonances for the $^1S^e$ and $^1P^o$ series, respectively, below the $N = 2$ (-0.5 au) threshold. Herrick's notation[101] has been used to label these doubly excited states $_N(K,T)_n^A$. Three of the eigenphases have been shifted in energy to better visualize the comparison of the resonant profile with the benchmark. E_{ref} and Γ_{ref} correspond to the reference values.
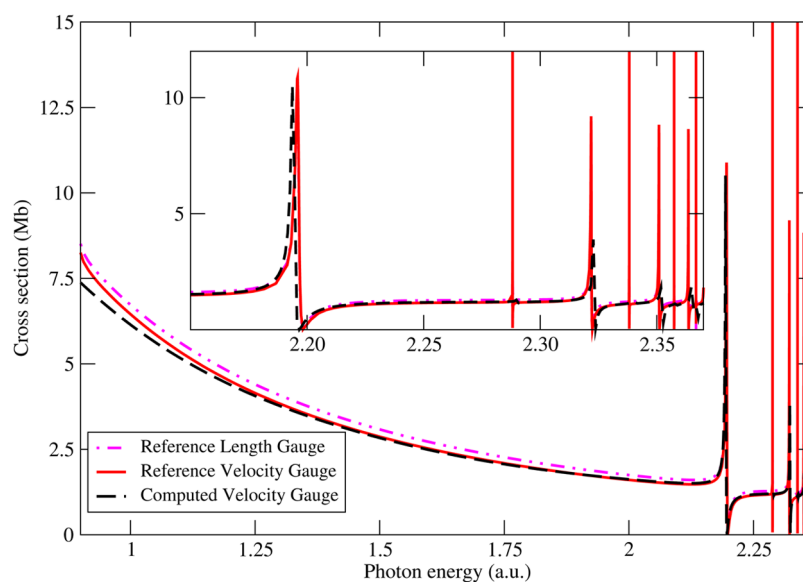
Figure 6. Cross-section from the He ground state. The inset shows the region where the first resonances appear, having the characteristic Fano profile.
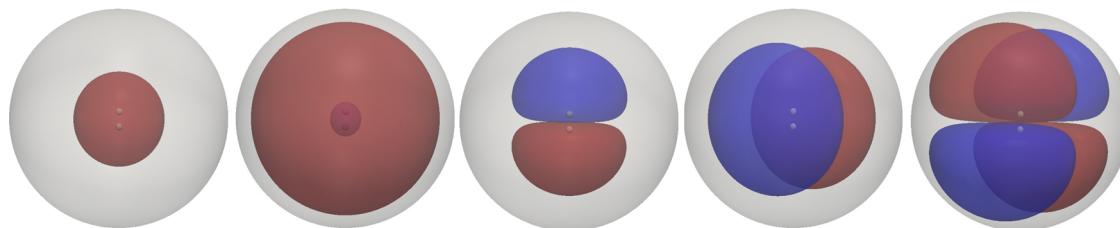

Figure 7. Orbitals included in the active space of the H_2^+ parent ion, from left to right: $1s\sigma_g$, $2s\sigma_g$, $2p\sigma_u$, $2p\pi_u$, and $3d\pi_g$. The sphere defining the region in which B-splines are not present is also shown.

those profiles corresponding to the channels in which the parent ion is left in the $He^+(1s)$ state, deviations from the reference results are larger than 5%. This is because the energy of the continuum electron coupled with the 1s parent ion is high (>1.5 au) and the chosen GABS basis is not flexible enough to provide an accurate representation of the corresponding rapidly oscillating continuum orbital. The agreement can be systematically improved, however, by increasing the number of K's in the monocentric Gaussian components of the GABS basis.

Figure 6 shows the photoionization cross-section below the $N = 2$ threshold, obtained by using eq 41 and the CC_3 ansatz. The calculated spectrum exhibits pronounced peaks corresponding to the resonances belonging to the $^1P^o$ series, which display the characteristic Fano line shapes.[36] Figure 6 also shows the comparison between our results in velocity gauge and those from the reference calculations in velocity and length gauges. The agreement between the two gauges within the benchmark and between the benchmark and our results is again very good.

4.2. Ionization of the H_2 Molecule. To test our model in a molecular target, we have chosen the simplest multielectronic molecule, H_2, for which one can compare with accurate benchmark calculations.[34,64]

In the calculations of the parent ion H_2^+, several states were obtained by using the CASSCF methodology with an active space of one electron in seven orbitals and the s and p functions from the aug-cc-pV6Z basis set.[102] The states included in the

parent-ion calculation were 2 for the symmetry A_g ($1s\sigma_g$ and $2s\sigma_g$), and 1 for each of the symmetries B_{3u} and B_{2u} ($2p\pi_u$), B_{1u} ($2p\sigma_u$), B_{2g} and B_{3g} ($3d\pi_g$). The orbitals obtained for these states are shown in Figure 7. As explained in section 3.1, the orbitals were optimized with the MOLPRO package using D_{2h} symmetry and exported to MOLCAS to carry out the augmentation procedure. In this case, the GUGA tables employed were a CAS(1,7) for the parent ion and a CAS(2,9) for the augmented states. For the GABS basis we used the same parametrization as for the helium atom (see previous section), except for the fact that this time the box radius is 200 au.

To assess the performance of the GABS basis for the description of molecular properties, we first compare the XCHEM results with those obtained from high-level QC methods. Due to the limitations of the latter in describing the ionization continuum, the comparison is restricted to bound states. In particular, we have compared the energies of the lowest $^1\Sigma_g^+$ and $^1\Sigma_u^+$ states of H_2, and the corresponding transition dipole moments between them at the equilibrium distance, obtained from (i) a standard MRCIS calculation with the s and p functions from the aug-cc-pV6Z basis set, (ii) the XCHEM calculation performed by augmenting the parent ions with the polycentric localized Gaussian orbitals only, (iii) the XCHEM calculation where both polycentric and diffuse monocentric Gaussian orbitals were included, and (iv) the XCHEM calculation performed with the localized Gaussian orbitals plus the whole GABS basis, i.e., the full XCHEM calculation. We notice that evaluation of transition dipole

matrix elements is a stringent test of the accuracy of the one-particle density matrix. The results are shown in Table 3.

Table 3. Energies and Transition Dipole Matrix Elements for the First Three $^1\Sigma_g^+$ and the First Two $^1\Sigma_u^+$ States of H_2 at the Equilibrium Distance ($R = 1.4$ au), Obtained from Four Different Computational Schemes[a]

	MRCIS	XCHEM-1[b]	XCHEM-2[c]	XCHEM[d]
		Energy (au)		
$^1\Sigma_g^+$	−1.1674	−1.1380	−1.1650	−1.1650
	−0.6908	−0.5682	−0.6905	−0.6905
	−0.5717	−0.0185	−0.6263	−0.6263
$^1\Sigma_u^+$	−0.7047	−0.5156	−0.7040	−0.7040
	−0.6159	0.0163	−0.6280	−0.6279
		Dipole (au)		
$1(^1\Sigma_g^+) - 1(^1\Sigma_u^+)$	0.4546	0.3643	0.4537	0.4530
$1(^1\Sigma_g^+) - 2(^1\Sigma_u^+)$	0.3105	0.0296	0.2145	0.2201
$2(^1\Sigma_g^+) - 1(^1\Sigma_u^+)$	0.0370	−0.1722	0.0382	0.0382
$2(^1\Sigma_g^+) - 2(^1\Sigma_u^+)$	0.1956	0.0140	0.1465	0.1468
$3(^1\Sigma_g^+) - 1(^1\Sigma_u^+)$	−0.1088	−0.0452	−0.1713	−0.1724
$3(^1\Sigma_g^+) - 2(^1\Sigma_u^+)$	−0.1595	0.0037	−0.0083	−0.0129

[a]In the multireference configuration interaction singles calculations (MRCIS), besides the active orbitals described in the text to obtain the parent-ion wave functions, we have also included the $3s\sigma_g$, $3p\pi_u$, $3p\sigma_u$, and $4d\pi_g$ orbitals. Using this approach, only single excitations were allowed. The other results have been obtained by using the XCHEM formalism at three different levels of approximation (see b, c, and d footnotes). The dipoles were calculated along the z direction in the velocity gauge. [b]Only polycentric Gaussian basis functions. [c]Polycentric and monocentric Gaussian basis functions. [d]All Gaussian basis functions plus B-spline functions.

Apart for the third $^1\Sigma_g^+$ and the second $^1\Sigma_u^+$ states, which are poorly represented in the MRCIS calculations due to the lack of diffuse functions, models i and iii yield nearly identical energies and dipoles. These findings show that the Gaussian basis set we use in our calculations is at least as accurate as that used in standard MRCI calculations. More importantly, the results of iii and iv show that the addition of B-spline functions has no effect on the energies and transition dipole elements. Therefore, we can safely conclude that the combination of polycentric Gaussian and GABS basis functions is as accurate as standard QC basis sets for the description of the lowest bound states and hence of the inner part of the molecular continuum.

To assess the quality of the XCHEM approach in describing the ionization continuum, we have performed calculations in the fixed-nuclei approximation for the first three $^1\Sigma_u^+$ resonances at several internuclear distances and compared them with those from an independent computation based on a different formalism,[34] which essentially leads to exact results. The CC ansatz used to build the $^1\Sigma_u^+$ channel from a collection of H_2^+ parent-ion states is

$$1s\sigma_g \otimes X_{l0}, \quad l = 0, 1, 2, 3$$
$$2p\sigma_u \otimes X_{l0}, \quad l = 0, 1, 2, 3$$
$$(2p\pi_u)_{x,y} \otimes X_{lm}, \quad l = 1, 2, 3, \quad m = \pm1$$
$$2s\sigma_g \otimes X_{l0}, \quad l = 0, 1, 2, 3$$
$$(3d\pi_g)_{x,y} \otimes X_{lm}, \quad l = 1, 2, 3, \quad m = \pm1$$

(42)

The results for the resonance positions and widths are given in Table 4. As can be seen, there is a good agreement for almost all the resonances. The larger discrepancies show up for the second and third resonances at an internuclear distance of 2.0 au, for which the resonance widths are ∼40% off. The second and third $^1\Sigma_u^+$ resonances are almost degenerate in a large interval of internuclear distances, and they exhibit a sharp avoided crossing.[34] As a consequence, even minor errors in their relative energy cause a major shift of the internuclear distance at which the crossing takes place, thus leading to large errors in the corresponding autoionization widths. Apart from this special case, the general trend is that the shorter the internuclear distance the better the accuracy, which is reasonable given that we are using the same monocentric Gaussian expansion for all radial distances.

Figure 8 shows the photoionization cross-section, from the ground $^1\Sigma_g^+$ state to the $^1\Sigma_u^+$ continuum in velocity gauge, at the equilibrium internuclear distance (1.4 au). The cross-section includes contributions from doubly excited states associated with our choice of the parent-ion states given in eq 42. In the figure, we only show the first resonance, which appears as a pronounced dip at around a photon energy of 1.13 au, in excellent agreement with earlier results in the fixed-nuclei approximation.[61,103] Using the code of ref 104, we have also performed all-B-spline reference calculations for the photoionization nonresonant background in which we included the same number of parent-ion states as in eq 42. These reference

Table 4. First Three $^1\Sigma_u^+$ Resonances Energies and Widths (au), for Several Internuclear Distances, R[a]

R	Resonance	E_{ref}	Γ_{ref}	E	Γ
1.0	1	0.2853	8.74(−3)	0.2847	8.94(−3)
1.0	2	0.3708	1.89(−3)	0.3703	1.97(−3)
1.0	3	0.3808	2.71(−4)	0.3809	2.86(−4)
1.4	1	−3.592(−2)	1.54(−2)	−3.602(−2)	1.45(−2)
1.4	2	4.237(−2)	3.58(−3)	4.206(−2)	3.89(−3)
1.4	3	4.794(−2)	6.21(−4)	4.792(−2)	5.88(−4)
2.0	1	−0.2926	2.55(−2)	−0.2899	2.33(−2)
2.0	2	−0.2236	3.52(−3)	−0.2225	1.39(−3)
2.0	3	−0.2212	3.94(−3)	−0.2223	6.45(−3)
3.0	1	−0.4783	4.10(−2)	−0.4673	3.67(−2)
3.0	2	−0.4238	2.80(−3)	−0.4230	2.21(−3)
3.0	3	−0.4177	1.15(−2)	−0.4170	9.73(−3)

[a]The results obtained with eq 42 CC ansatz are compared with accurate reference results taken from ref 34. Numbers in parentheses represent power of 10.
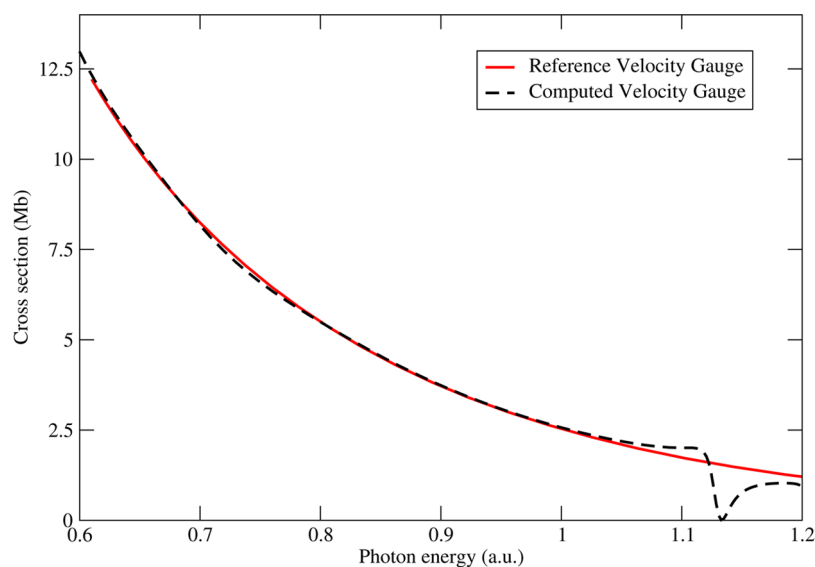
Figure 8. Photoionization cross-section from the H_2 ground state at equilibrium distance to the $^1\Sigma_u^+$ continuum. The reference (see text for details) does not include the resonances (only the background); meanwhile the present computation does include the resonances, the first of which is shown.

calculations do not include the contribution from the doubly excited states and lead essentially to results that are nearly indistinguishable from those reported in ref 61 for the nonresonant background. Except for the obvious absence of the resonance in the latter calculations, the agreement with our results is excellent.

4.3. Extension to Larger Systems. Application of the XCHEM code to larger molecules is straightforward, and the increase in computational time with respect to, e.g., H_2 should be similar to that experienced in bound-state calculations for the same systems. This is due to the quite different sizes of the polycentric and monocentric Gaussian bases used to describe, respectively, the short-range part of the wave function and its transition to the asymptotic region (the $[R_0, R_1]$ interval in Figure 2). Typically, in calculations aiming at describing ionization, the monocentric basis should contain, as in the present work, ~400 functions, leading to $N_m \sim 200$ orbitals after removing linear dependencies. In contrast, a 6Z polycentric Gaussian basis, which is among the largest ones contains ~30 functions per atom, leading to $N_c \sim 10$ orbitals per atom in both active and inactive spaces. The large monocentric basis enters the calculation through the augmentation procedure described in section 3.3, which is thus the most expensive part of the calculation. When moving from H_2 to a larger molecule, *only* the number of polycentric Gaussian functions has to be increased and, therefore, the cost of augmentation remains more or less the same. Indeed, for a molecule containing N atoms, the size of the basis is approximately given by the formula $N_m + N \times N_c$. Since N_m is big, one has to go to a rather high N to observe a significant increase in computational time associated with the augmentation procedure. For example, for GABS bases similar to those used in the present work, this is expected to occur when $N_m \simeq N \times N_c$, i.e., for $N \sim 20$.

5. CONCLUSIONS

One of the main limitations of existing QCPs is their inability to describe the electronic continuum of molecules, which for many years has limited the study of molecular ionization

processes. In this work, we have merged existing QCPs and state-of-the-art numerical scattering methods to overcome this limitation. The new method follows the spirit of earlier close-coupling approaches, in which the scattering wave function is expanded in a basis of channel states representing a molecular cation in a given electronic state and a continuum electron satisfying the appropriate scattering boundary conditions. The electronic configuration space is divided into a short-range region, where electronic configurations are built in terms of Gaussian functions compatible with QCPs, and a long-range region, where a single electron interacts with a finite number of correlated molecular-ion states. The state of this electron is expressed in terms of the hybrid-basis GABS, which combines monocentric Gaussian functions with B-splines appropriate to represent the continuum. As a first step toward more complex systems, we have illustrated the performance of this method in multichannel ionization of He and H_2 by comparing with results from nearly exact ad hoc computational methods available in the literature for such simple systems.

Our method takes advantage of existing ab initio quantum chemistry packages such as MOLCAS and MOLPRO, thus putting their advanced machinery at our disposal and facilitating its widespread use by chemical physicists. This is in contrast with ongoing developments,[76] in which both the short-range and long-range parts of the scattering wave function are described by the same kind of basis functions, usually chosen to provide a good description of the continuum electron but offering much less flexibility for the description of the many-electron wave function in the molecular region. Other computational approaches combining ab initio quantum chemistry and scattering methods are currently under development,[30,71−75] but, at variance with them, our method is able to include electron correlation and exchange in the electronic continuum at the same level of accuracy as quantum chemistry does for bound states. Another important advantage is that increasing the number of electrons for a fixed number of scattering channels does not increase the computational cost of the full dimensional problem significantly. In other words, the effort made to evaluate the electronic continuum in, let us say,

H$_2$, would be similar to that required for a polyatomic molecule such as water or acetylene. Finally, the present method also allows us to describe ionization in many-electron atoms, again taking advantage of many of the features that QCPs incorporate and that are not so often available in atomic computational codes.

Applications of our method to describe ionization in more complicated systems, such as Ne, N$_2$, CO, and H$_2$O, are currently in progress in our laboratory.

■ APPENDIX: MATRIX ELEMENTS BETWEEN EXTENDED CHANNEL FUNCTIONS REPRESENTED WITH GABS BASIS FUNCTIONS

The matrix element of a totally symmetric operator O between extended channel functions is

$$O_{\alpha i,\beta j} = \langle \bar{\Upsilon}_{\alpha i}|O|\bar{\Upsilon}_{\beta j}\rangle = \frac{N_{\alpha i}^* N_{\beta j}}{N_e}\langle \Upsilon_\alpha \varphi_i|O\left(1 - \sum_{i=1}^{N_e-1}\mathcal{P}_{iN_e}\right)|\Upsilon_\beta \varphi_j\rangle \tag{43}$$

where we have made use of the hermiticity and idempotency of the antisymmetrizer ($\hat{\mathcal{A}}^\dagger = \hat{\mathcal{A}}$, $\hat{\mathcal{A}}^2 = \hat{\mathcal{A}}$) and of the invariance of the operator O with respect to permutations ($\forall\,\mathcal{P} \in S_{N_e}$, $[O,\mathcal{P}] = 0 \Rightarrow [O,\hat{\mathcal{A}}] = 0$). If either φ_i or φ_j have disjoint support from those of the parent ions, the permutation operators in eq 43 can be dropped

$$O_{\alpha i,\beta j} = \langle \bar{\Upsilon}_{\alpha i}|O|\bar{\Upsilon}_{\beta j}\rangle = \frac{N_{\alpha i}^* N_{\beta j}}{N_e}\langle \Upsilon_\alpha \varphi_i|O|\Upsilon_\beta \varphi_j\rangle,$$
$$\text{if } \varphi_i(r) = 0 \vee \varphi_j(r) = 0,\, \forall\, r < R_0 \tag{44}$$

In the latter condition, the overlap, monoelectronic and bielectronic interchannel matrix elements ($\alpha = al_\alpha m_\alpha$, $\beta = bl_\beta m_\beta$) have simple expressions, as given below.

Overlap Matrix Elements

$$S_{\alpha i,\beta j} = \langle \bar{\Upsilon}_{\alpha i}|\bar{\Upsilon}_{\beta j}\rangle = \frac{N_{\alpha i}^* N_{\beta j}}{N_e}\langle \Upsilon_\alpha|\Upsilon_\beta\rangle\langle \varphi_i|\varphi_j\rangle = \frac{N_{\alpha i}^* N_{\beta j}}{N_e}\delta_{\alpha\beta}s_{ij} \tag{45}$$

where $\delta_{\alpha\beta} = \delta_{ab}\delta_{l_\alpha l_\beta}\delta_{m_\alpha m_\beta}$ and $s_{ij} = \langle \varphi_i|\varphi_j\rangle$.

Mono-electronic Operators

These operators can be written as

$$T = \sum_{i=1}^{N_e} t(i) \tag{46}$$

and the corresponding matrix elements

$$T_{\alpha i,\beta j} = \frac{N_{\alpha i}^* N_{\beta j}}{N_e}(T_{ab}\delta_{l_\alpha l_\beta}\delta_{m_\alpha m_\beta}s_{ij} + \delta_{ab}t_{l_\alpha m_\alpha i, l_\beta m_\beta j}) \tag{47}$$

where $T_{ab} = \langle \Phi_a|T|\Phi_b\rangle$ and $t_{lmi,l'm'j} = \langle \varphi_i Y_{lm}|t|\varphi_j Y_{l'm'}\rangle$. The matrix elements T_{ab} can be obtained from the QCPs.

Hamiltonian Matrix Elements

The total electrostatic Hamiltonian is given by

$$H = K + V^{ee} + V^{ne} + V^{nn} \tag{48}$$

where $V^{nn} = \sum_{A,B>A} Z_A Z_B/R_{AB}$ is the nuclear repulsion potential, K is the kinetic energy operator, V^{en} is the electron−nuclei interaction potential,

$$V^{en} = -\sum_{i=1}^{N_e}\sum_{A=1}^{N_n}\frac{Z_A}{r_{iA}} \tag{49}$$

and V^{ee} is the electron−electron repulsion potential,

$$V^{ee} = \sum_{i,j>i}\frac{1}{r_{ij}} \tag{50}$$

The corresponding matrix element has the form

$$H_{\alpha i,\beta j} = \frac{N_{\alpha i}^* N_{\beta j}}{N_e}[H_{ab}\delta_{l_\alpha l_\beta}\delta_{m_\alpha m_\beta}s_{ij} + \delta_{ab}\delta_{l_\alpha l_\beta}\delta_{m_\alpha m_\beta}k_{i,j}^{(l_\alpha)}$$
$$+ \sum_{lm}\langle Y_{l_\alpha m_\alpha}Y_{lm}|Y_{l_\beta m_\beta}\rangle\langle \varphi_i|r^{-l-1}|\varphi_j\rangle M_{ab}^{mol,lm}] \tag{51}$$

where $M_{ab}^{mol,lm}$ is the molecular transition multipole given by

$$M_{ab}^{mol,lm} = M_{ab}^{el,lm} + M_{ab}^{nuc,lm} \tag{52}$$

$M_{ab}^{el,lm}$ being the electronic transition multipole,

$$M_{ab}^{el,lm} = \frac{4\pi}{2l+1}\langle \Phi_a|\sum_{i=1}^{N_e-1} r_i^l Y_{lm}(\hat{r}_i)|\Phi_b\rangle$$
$$= \frac{4\pi(N_e-1)}{2l+1}\langle \Phi_a|r_1^l Y_{lm}(\hat{r}_1)|\Phi_b\rangle \tag{53}$$

and $M_{ab}^{nuc,lm}$ the nuclear transition multipole,

$$M_{ab}^{nuc,lm} = -\frac{4\pi}{2l+1}\delta_{ab}\sum_{A=1}^{N_n} Z_A R_A^l Y_{lm}^*(\hat{R}_A) \tag{54}$$

The matrix elements H_{ab} and $M_{ab}^{mol,lm}$ are obtained from the QCPs. Notice that the monopole term has the simple form

$$M_{ab}^{mol,00} = \sqrt{4\pi}\delta_{ab}Q \tag{55}$$

where Q is the total charge of the parent ion. Notice also that, in order for the scattering theory to be applicable, the channels must be asymptotically decoupled, i.e., the parent-ion states must diagonalize the $N_e - 1$ molecular Hamiltonian

$$H_{ab} = E_a\delta_{ab} \tag{56}$$

If we define the hydrogenic mono-electronic operator h as

$$h_{i,j}^{(l)} = k_{i,j}^{(l)} + Q\langle \varphi_i|r^{-1}|\varphi_j\rangle \tag{57}$$

we can rewrite the expression for the Hamiltonian matrix elements by explicitly indicating the contribution of the multipoles with $l > 0$ only

$$H_{\alpha i,\beta j} = \frac{N_{\alpha i}^* N_{\beta j}}{N_e}[(E_a s_{ij} + h_{i,j}^{(l_\alpha)})\delta_{ab}\delta_{l_\alpha l_\beta}\delta_{m_\alpha m_\beta}$$
$$+ \sum_{l>0,m}\langle Y_{l_\alpha m_\alpha}Y_{lm}|Y_{l_\beta m_\beta}\rangle\langle \varphi_i|r^{-l-1}|\varphi_j\rangle M_{ab}^{mol,lm}] \tag{58}$$

Other Matrix Elements

For completeness we also provide the expressions for the matrix elements of the electron−nucleus and electron−electron interactions potentials. For the former, the matrix element is given by

$$V_{\alpha i,\beta j}^{en} = \frac{N_{\alpha i}^* N_{\beta j}}{N_e}[V_{ab}^{en}\delta_{l_d l_f}\delta_{m_\alpha m_\beta}s_{ij} + \sum_{lm}\langle Y_{l_\alpha m_\alpha}Y_{lm}|Y_{l_\beta m_\beta}\rangle$$
$$\langle\varphi_i|r^{-l-1}|\varphi_j\rangle M_{ab}^{nuc,lm}] \tag{59}$$

where the integral of three harmonics has the following expression

$$\langle Y_{a\alpha}Y_{b\beta}|Y_{c\gamma}\rangle = \sqrt{\frac{(2a+1)(2b+1)}{4\pi(2c+1)}}C_{a0,b0}^{c0}C_{a\alpha,b\beta}^{c\gamma} \tag{60}$$

and for the latter,

$$V_{\alpha i,\beta j}^{ee} = \frac{N_{\alpha i}^* N_{\beta j}}{N_e}[V_{ab}^{ee}\delta_{l_d l_f}\delta_{m_\alpha m_\beta}s_{ij} + \sum_{lm}\langle Y_{l_\alpha m_\alpha}Y_{lm}|Y_{l_\beta m_\beta}\rangle$$
$$\langle\varphi_i|r^{-l-1}|\varphi_j\rangle M_{ab}^{el,lm}] \tag{61}$$

■ AUTHOR INFORMATION

Corresponding Authors
*(J.G.-V.) E-mail: jesus.gonzalezv@uam.es.
*(F.M.) E-mail: fernando.martin@uam.es.

ORCID
Jesús González-Vázquez: 0000-0003-2204-3549

Notes
The authors declare no competing financial interest.

■ ACKNOWLEDGMENTS

■ REFERENCES

(1) Schöffler, M.; Titze, J.; Petridis, N.; Jahnke, T.; Cole, K.; Schmidt, L. P. H.; Czasch, A.; Akoury, D.; Jagutzki, O.; Williams, J. B.; Cherepkov, N. A.; Semenov, S. K.; McCurdy, C. W.; Rescigno, T. N.; Cocke, C. L.; Osipov, T.; Lee, S.; Prior, M. H.; Belkacem, A.; Landers, A. L.; Schmidt-Böcking, H.; Weber, T.; Dörner, R. *Science* **2008**, *320*, 920−923.

(2) Jahnke, T.; Sann, H.; Havermeier, T.; Kreidi, K.; Stuck, C.; Meckel, M.; Schöffler, M.; Neumann, N.; Wallauer, R.; Voss, S.; Czasch, A.; Jagutzki, O.; Malakzadeh, A.; Afaneh, F.; Weber, T.; Dörner, R. D.; Schmidt-Böcking, H. *Nat. Phys.* **2010**, *6*, 139−142.

(3) Dell'Angela, M.; Anniyev, T.; Beye, M.; Coffee, R.; Fohlisch, A.; Gladh, J.; Katayama, T.; Kaya, S.; Krupin, O.; LaRue, J.; Mogelhoj, A.; Nordlund, D.; Norskov, J. K.; Oberg, H.; Ogasawara, H.; Ostrom, H.; Pettersson, L. G. M.; Schlotter, W. F.; Sellberg, J. a.; Sorgenfrei, F.; Turner, J. J.; Wolf, M.; Wurth, W.; Nilsson, A. *Science* **2013**, *339*, 1302−1305.

(4) Calegari, F.; Ayuso, D.; Trabattoni, A.; Belshaw, L.; De Camillis, S.; Anumula, S.; Frassetto, F.; Poletto, L.; Palacios, A.; Decleva, P.; Greenwood, J. B.; Martín, F.; Nisoli, M. *Science* **2014**, *346*, 336−339.

(5) Ott, C.; Kaldun, A.; Argenti, L.; Raith, P.; Meyer, K.; Laux, M.; Zhang, Y.; Blättermann, A.; Hagstotz, S.; Ding, T.; Heck, R.; Madroñero, J.; Martín, F.; Pfeifer, T. *Nature* **2014**, *516*, 374−378.

(6) Månsson, E. P.; Guénot, D.; Arnold, C. L.; Kroon, D.; Kasper, S.; Dahlström, J. M.; Lindroth, E.; Kheifets, A. S.; L'Huillier, A.; Sorensen, S. L.; Gisselbrecht, M. *Nat. Phys.* **2014**, *10*, 207−211.

(7) Kraus, P. M.; Mignolet, B.; Baykusheva, D.; Rupenyan, A.; Horný, L.; Penka, E. F.; Grassi, G.; Tolstikhin, O. I.; Schneider, J.; Jensen, F.; Madsen, L. B.; Bandrauk, A. D.; Remacle, F.; Wörner, H. J. *Science* **2015**, *350*, 790−795.

(8) Nisoli, M.; Calegari, F.; Palacios, A.; Decleva, P.; Martín, F. *Chem. Rev.* **2016**, to be submitted for publication.

(9) McNeil, B. W. J.; Thompson, N. R. *Nat. Photonics* **2010**, *4*, 814−821.

(10) Krausz, F.; Ivanov, M. *Rev. Mod. Phys.* **2009**, *81*, 163−234.

(11) Chini, M.; Zhao, K.; Chang, Z. *Nat. Photonics* **2014**, *8*, 178−186.

(12) Lambert, G.; Hara, T.; Garzella, D.; Tanikawa, T.; Labat, M.; Carre, B.; Kitamura, H.; Shintake, T.; Bougeard, M.; Inoue, S.; Tanaka, Y.; Salieres, P.; Merdji, H.; Chubar, O.; Gobert, O.; Tahara, K.; Couprie, M.-E. *Nat. Phys.* **2008**, *4*, 296−300.

(13) Allaria, E.; Appio, R.; Badano, L.; Barletta, W. A.; Bassanese, S.; Biedron, S. G.; Borga, A.; Busetto, E.; Castronovo, D.; Cinquegrana, P.; Cleva, S.; Cocco, D.; Cornacchia, M.; Craievich, P.; Cudin, I.; D'Auria, G.; Dal Forno, M.; Danailov, M. B.; De Monte, R.; De Ninno, G.; Delgiusto, P.; Demidovich, A.; Di Mitri, S.; Diviacco, B.; Fabris, A.; Fabris, R.; Fawley, W.; Ferianis, M.; Ferrari, E.; Ferry, S.; Froehlich, L.; Furlan, P.; Gaio, G.; Gelmetti, F.; Giannessi, L.; Giannini, M.; Gobessi, R.; Ivanov, R.; Karantzoulis, E.; Lonza, M.; Lutman, A.; Mahieu, B.; Milloch, M.; Milton, S. V.; Musardo, M.; Nikolov, I.; Noe, S.; Parmigiani, F.; Penco, G.; Petronio, M.; Pivetta, L.; Predonzani, M.; Rossi, F.; Rumiz, L.; Salom, A.; Scafuri, C.; Serpico, C.; Sigalotti, P.; Spampinati, S.; Spezzani, C.; Svandrlik, M.; Svetina, C.; Tazzari, S.; Trovo, M.; Umer, R.; Vascotto, A.; Veronese, M.; Visintini, R.; Zaccaria, M.; Zangrando, D.; Zangrando, M. *Nat. Photonics* **2012**, *6*, 699−704.

(14) Gauthier, D.; Ribič, P. R.; De Ninno, G.; Allaria, E.; Cinquegrana, P.; Danailov, M. B.; Demidovich, A.; Ferrari, E.; Giannessi, L.; Mahieu, B.; Penco, G. *Phys. Rev. Lett.* **2015**, *115*, 114801.

(15) Žitnik, M.; Mihelič, A.; Bučar, K.; Kavčič, M.; Rubensson, J.-E.; Svanquist, M.; Söderström, J.; Feifel, R.; Såthe, C.; Ovcharenko, Y.; Lyamayev, V.; Mazza, T.; Meyer, M.; Simon, M.; Journel, L.; Lüning, J.; Plekan, O.; Coreno, M.; Devetta, M.; Di Fraia, M.; Finetti, P.; Richter, R.; Grazioli, C.; Prince, K. C.; Callegari, C. *Phys. Rev. Lett.* **2014**, *113*, 193201.

(16) Silva, F.; Teichmann, S. M.; Cousin, S. L.; Hemmer, M.; Biegert, J. *Nat. Commun.* **2015**, *6*, 6611.

(17) Arbelo-González, W.; Crespo-Otero, R.; Barbatti, M. *J. Chem. Theory Comput.* **2016**, *12*, 5037−5049.

(18) Gozem, S.; Gunina, A. O.; Ichino, T.; Osborn, D. L.; Stanton, J. F.; Krylov, A. I. *J. Phys. Chem. Lett.* **2015**, *6*, 4532−4540.

(19) Corrales, M. E.; González-Vázquez, J.; Balerdi, G.; Solá, I. R.; de Nalda, R.; Bañares, L. *Nat. Chem.* **2014**, *6*, 785−790.

(20) Shelby, M. L.; Lestrange, P. J.; Jackson, N. E.; Haldrup, K.; Mara, M. W.; Stickrath, A. B.; Zhu, D.; Lemke, H.; Chollet, M.; Hoffman, B. M.; Li, X.; Chen, L. X. *J. Am. Chem. Soc.* **2016**, *138*, 8752−8764.

(21) Burke, P. G. *R-Matrix Theory of Atomic Collisions. Application to Atomic, Molecular and Optical Processes*; Springer Series on Atomic, Optical, and Plasma Physics; Springer-Verlag; Heidelberg, Germany, 2011; Vol. 61.

(22) Tennyson, J. *Phys. Rep.* **2010**, *491*, 29−76.

(23) Zatsarinny, O.; Bartschat, K. *J. Phys. B: At, Mol. Opt. Phys.* **2013**, *46*, 112001.

(24) Argenti, L.; Pazourek, R.; Feist, J.; Nagele, S.; Liertzer, M.; Persson, E.; Burgdörfer, J.; Lindroth, E. *Phys. Rev. A: At., Mol., Opt. Phys.* **2013**, *87*, 053405.

(25) Carette, T.; Dahlström, J. M.; Argenti, L.; Lindroth, E. *Phys. Rev. A: At., Mol., Opt. Phys.* **2013**, *87*, 023420.

(26) Awasthi, M.; Vanne, Y. V.; Saenz, A.; Castro, A.; Decleva, P. *Phys. Rev. A: At., Mol., Opt. Phys.* **2008**, *77*, 063403.

(27) Kukk, E.; Ayuso, D.; Thomas, T. D.; Decleva, P.; Patanen, M.; Argenti, L.; Plésiat, E.; Palacios, A.; Kooser, K.; Travnikova, O.; Mondal, S.; Kimura, M.; Sakai, K.; Miron, C.; Martín, F.; Ueda, K. *Phys. Rev. A: At., Mol., Opt. Phys.* **2013**, *88*, 033412.

(28) Ayuso, D.; Palacios, A.; Decleva, P.; Martín, F. *J. Electron Spectrosc. Relat. Phenom.* **2014**, *195*, 320−326.

(29) Hättig, C.; Klopper, W.; Köhn, A.; Tew, D. P. *Chem. Rev.* **2012**, *112*, 4−74.

(30) Nguyen-Dang, T.-T.; Couture-Bienvenue, É; Viau-Trudel, J.; Sainjon, A. *J. Chem. Phys.* **2014**, *141*, 244116.

(31) Tashiro, M.; Ueda, K.; Ehara, M. *J. Chem. Phys.* **2011**, *135*, 154307.

(32) Aksela, H.; Aksela, S. *Radiat. Phys. Chem.* **2007**, *76*, 370−374.

(33) Liu, J. C.; Nicolas, C.; Sun, Y. P.; Flammini, R.; O'Keeffe, P.; Avaldi, L.; Morin, P.; Kimberg, V.; Kosugi, N.; Gel'mukhanov, F.; Miron, C. *J. Phys. Chem. B* **2011**, *115*, 5103−5112.

(34) Sánchez, I.; Martín, F. *J. Chem. Phys.* **1997**, *106*, 7720.

(35) Kopelke, S.; Gokhberg, K.; Cederbaum, L. S.; Averbukh, V. *J. Chem. Phys.* **2009**, *130*, 144103.

(36) Fano, U. *Phys. Rev.* **1961**, *124*, 1866−1878.

(37) Carravetta, V.; Ågren, H.; Vahtras, O.; Jensen, H. J. A. *J. Chem. Phys.* **2000**, *113*, 7790.

(38) Tashiro, M.; Ueda, K.; Ehara, M. *Chem. Phys. Lett.* **2012**, *521*, 45−51.

(39) Tian, Q.; Yang, J.; Shi, Y.; Shan, X.; Chen, X. *J. Chem. Phys.* **2012**, *136*, 094306.

(40) Sukiasyan, S.; Patchkovskii, S.; Smirnova, O.; Brabec, T.; Ivanov, M. Y. *Phys. Rev. A: At., Mol., Opt. Phys.* **2010**, *82*, 043414.

(41) Pisanty, E.; Ivanov, M. *Phys. Rev. A: At., Mol., Opt. Phys.* **2014**, *89*, 043416.

(42) Badnell, N. R.; Bautista, M. A.; Butler, K.; Delahaye, F.; Mendoza, C.; Palmeri, P.; Zeippen, C. J.; Seaton, M. J. *Mon. Not. R. Astron. Soc.* **2005**, *360*, 458−464.

(43) Boudaïffa, B.; Cloutier, P.; Hunting, D.; Huels, M. A.; Sanche, L. *Science* **2000**, *287*, 1658−1660.

(44) Dörner, R.; Mergel, V.; Jagutzki, O.; Spielberger, L.; Ullrich, J.; Moshammer, R.; Schmidt-Böcking, H. *Phys. Rep.* **2000**, *330*, 95−192.

(45) Eppink, A. T. J. B.; Parker, D. H. *Rev. Sci. Instrum.* **1997**, *68*, 3477−3484.

(46) Lindle, D. W.; Hemmers, O. A. *J. Alloys Compd.* **2001**, *328*, 27−34.

(47) Goulielmakis, E.; Loh, Z.-H.; Wirth, A.; Santra, R.; Rohringer, N.; Yakovlev, V. S.; Zherebtsov, S.; Pfeifer, T.; Azzeer, A. M.; Kling, M. F.; Leone, S. R.; Krausz, F. *Nature* **2010**, *466*, 739−743.

(48) Schmidt, V. *Rep. Prog. Phys.* **1992**, *55*, 1483−1659.

(49) Bilderback, D. H.; Elleaume, P.; Weckert, E. *J. Phys. B: At., Mol. Opt. Phys.* **2005**, *38*, S773−S797.

(50) Canton, S. E.; Plésiat, E.; Bozek, J. D.; Rude, B. S.; Decleva, P.; Martín, F. *Proc. Natl. Acad. Sci. U. S. A.* **2011**, *108*, 7302−7306.

(51) Ueda, K.; Miron, C.; Plésiat, E.; Argenti, L.; Patanen, M.; Kooser, K.; Ayuso, D.; Mondal, S.; Kimura, M.; Sakai, K.; Travnikova, O.; Palacios, A.; Decleva, P.; Kukk, E.; Martín, F. *J. Chem. Phys.* **2013**, *139*, 124306.

(52) Wuilleumier, F. J.; Meyer, M. *J. Phys. B: At., Mol. Opt. Phys.* **2006**, *39*, R425−R477.

(53) Szalay, P. G.; Müller, T.; Gidofalvi, G.; Lischka, H.; Shepard, R. *Chem. Rev.* **2012**, *112*, 108−181.

(54) Saito, N.; Toffoli, D.; Lucchese, R. R.; Nagoshi, M.; De Fanis, A.; Tamenori, Y.; Oura, M.; Yamaoka, H.; Kitajima, M.; Tanaka, H.; Hergenhahn, U.; Ueda, K. *Phys. Rev. A: At., Mol., Opt. Phys.* **2004**, *70*, 062724.

(55) Plésiat, E.; Decleva, P.; Martín, F. *J. Phys. B: At., Mol. Opt. Phys.* **2012**, *45*, 194008.

(56) Padial, N.; Csanak, G.; McKoy, B. V.; Langhoff, P. W. *Phys. Rev. A: At., Mol., Opt. Phys.* **1981**, *23*, 218−235.

(57) McKoy, V.; Carlson, T. A.; Lucchese, R. R. *J. Phys. Chem.* **1984**, *88*, 3188−3196.

(58) Burke, P. G.; Schey, H. M. *Phys. Rev.* **1962**, *126*, 147−162.

(59) Cacelli, I.; Moccia, R.; Rizzo, A. *J. Chem. Phys.* **1995**, *102*, 7131−7141.

(60) Cacelli, I.; Moccia, R.; Rizzo, A. *Chem. Phys.* **2000**, *252*, 67−81.

(61) Martín, F. *J. Phys. B: At., Mol. Opt. Phys.* **1999**, *32*, R197−R231.

(62) Bachau, H.; Cormier, E.; Decleva, P.; Hansen, J. E.; Martín, F. *Rep. Prog. Phys.* **2001**, *64*, 1815−1943.

(63) Rescigno, T. N.; McCurdy, C. W. *Phys. Rev. A: At., Mol., Opt. Phys.* **2000**, *62*, 032706.

(64) Sánchez, I.; Martín, F. *J. Phys. B: At., Mol. Opt. Phys.* **1997**, *30*, 679−692.

(65) Vanne, Y. V.; Saenz, A.; Dalgarno, A.; Forrey, R. C.; Froelich, P.; Jonsell, S. *Phys. Rev. A: At., Mol., Opt. Phys.* **2006**, *73*, 062706.

(66) Vanroose, W.; Horner, D. A.; Martín, F.; Rescigno, T. N.; McCurdy, C. W. *Phys. Rev. A: At., Mol., Opt. Phys.* **2006**, *74*, 052702.

(67) Tao, L.; McCurdy, C. W.; Rescigno, T. N. *Phys. Rev. A: At., Mol., Opt. Phys.* **2010**, *82*, 023423.

(68) Aquilante, F.; Autschbach, J.; Carlson, R. K.; Chibotaru, L. F.; Delcey, M. G.; De Vico, L.; Galván, I. F.; Ferré, N.; Frutos, L. M.; Gagliardi, L.; Garavelli, M.; Giussani, A.; Hoyer, C. E.; Li Manni, G.; Lischka, H.; Ma, D.; Malmqvist, P. Å.; Müller, T.; Nenov, A.; Olivucci, M.; Pedersen, T. B.; Peng, D.; Plasser, F.; Pritchard, B.; Reiher, M.; Rivalta, I.; Schapiro, I.; Segarra-Martí, J.; Stenrup, M.; Truhlar, D. G.; Ungur, L.; Valentini, A.; Vancoillie, S.; Veryazov, V.; Vysotskiy, V. P.; Weingart, O.; Zapata, F.; Lindh, R. *J. Comput. Chem.* **2016**, *37*, 506−541.

(69) Werner, H.-J.; Knowles, P. J.; Knizia, G.; Manby, F. R.; Schütz, M. *WIREs Comput. Mol. Sci.* **2012**, *2*, 242−253.

(70) Marante, C.; Argenti, L.; Martín, F. *Phys. Rev. A: At., Mol., Opt. Phys.* **2014**, *90*, 012506.

(71) Majety, V. P.; Scrinzi, A. *Phys. Rev. Lett.* **2015**, *115*, 103002.

(72) Majety, V. P.; Scrinzi, A. *Photonics* **2015**, *2*, 93−103.

(73) Rescigno, T. N.; Horner, D. A.; Yip, F. L.; McCurdy, C. W. *Phys. Rev. A: At., Mol., Opt. Phys.* **2005**, *72*, 0052709.

(74) Yip, F. L.; McCurdy, C. W.; Rescigno, T. N. *Phys. Rev. A: At., Mol., Opt. Phys.* **2008**, *78*, 023405.

(75) Yip, F. L.; McCurdy, C. W.; Rescigno, T. N. *Phys. Rev. A: At., Mol., Opt. Phys.* **2014**, *90*, 063421.

(76) Toffoli, D.; Stener, M.; Fronzoni, G.; Decleva, P. *Chem. Phys.* **2002**, *276*, 25−43.

(77) Tong, X.-M.; Chu, S.-I. *Phys. Rev. A: At., Mol., Opt. Phys.* **1997**, *55*, 3406−3416.

(78) Abu-samha, M.; Madsen, L. B. *Phys. Rev. A: At., Mol., Opt. Phys.* **2010**, *81*, 033416.

(79) Beck, M. *Phys. Rep.* **2000**, *324*, 1−105.

(80) Kulander, K. *Phys. Rev. A: At., Mol., Opt. Phys.* **1987**, *35*, 445−447.

(81) Schirmer, J.; Braunstein, M.; McKoy, V. *Phys. Rev. A: At., Mol., Opt. Phys.* **1990**, *41*, 283−300.

(82) Lucchese, R. R.; Zurales, R. W. *Phys. Rev. A: At., Mol., Opt. Phys.* **1991**, *44*, 291−303.

(83) Caillat, J.; Zanghellini, J.; Kitzler, M.; Koch, O.; Kreuzer, W.; Scrinzi, A. *Phys. Rev. A: At., Mol., Opt. Phys.* **2005**, *71*, 012712.

(84) Toffoli, D.; Decleva, P. *J. Phys. B: At., Mol. Opt. Phys.* **2013**, *46*, 145101.

(85) Stener, M.; Decleva, P. *J. Electron Spectrosc. Relat. Phenom.* **1998**, *94*, 195−209.

(86) Rodberg, L. S.; Thaler, R. M. The S Matrix and the K Matrix. *Introduction to the Quantum Theory of Scattering*, 1st ed.; Academic Press: New York, 1967; pp 227−248.

(87) Friedrich, H. Elastic Scattering by a Conservative Potential. *Scattering Theory*, 1st ed.; Lecture Notes in Physics; Springer: Heidelberg, Germany, 2013; Vol. *872*; pp 23−130, DOI: 10.1007/978-3-642-38282-6_2.

(88) Hinze, J., Ed. The Graphical Unitary Group Approach and its Application to Direct Configuration Interaction Calculations. *The Unitary Group for the Evaluation of Electronic Energy Matrix Elements*, 1st ed.; Lecture Notes in Chemistry; Springer-Verlag: Heidelberg, Germany, 1981; Vol. *22*, pp 51−99, DOI: 10.1007/978-3-642-93163-5_2.

(89) Helgaker, T.; Jørgensen, P.; Olsen, J. Second Quantization. *Molecular Electronic-Structure Theory*, 1st ed.; John Wiley & Sons: Chichester, England, 2000; pp 1−32.

(90) Roos, B. O. The Complete Active Space Self-Consistent Field Method and its Applications in Electronic Structure Calculations. In *Ab Initio Methods in Quantum Chemistry Part 2*, 1st ed.; Lawley, K. P., Ed.; Advances in Chemical Physics; John Wiley & Sons: Chichester, England, 1987; Vol. 69; pp 399−445, DOI: 10.1002/9780470142943.ch7.

(91) Roos, B. O., Karlström, G., Malmqvist, P. Å., Sadlej, A. J. MOLCAS: A General Purpose Quantum Chemistry Program System for Correlated Wavefunctions. In *Modern techniques in computational chemistry: MOTECC-91*; Clementi, E., Ed.; ESCOM Science: New York, 1991; pp 435−453.

(92) Chisholm, C. D. H. *Group theoretical techniques in quantum chemistry*; Theoretical chemistry: A series of monographs; Academic Press: London, 1976; Vol. 5.

(93) de Boor, C. The Representation of PP Functions by B-Splines. *A Practical Guide to Splines*, revised ed.; Applied Mathematical Sciences; Springer-Verlag: New York, 2001; Vol. 27; pp 87−106.

(94) Feuerbacher, S.; Santra, R. *J. Chem. Phys.* **2005**, *123*, 194310.

(95) Argenti, L.; Colle, R. *Comput. Phys. Commun.* **2009**, *180*, 1442−1447.

(96) Abramowitz, M., Stegun, I. A., Eds. Coulomb Wave Functions. In *Handbook of Mathematical Functions: with Formulas, Graphs, and Mathematical Tables*, 10th ed.; Applied Mathematics Series; National Bureau of Standards: Washington D.C., 1972; Vol. 55; pp 537−554.

(97) Weidenmüller, H. *Phys. Lett. B* **1967**, *24*, 441−442.

(98) Hazi, A. U. *Phys. Rev. A: At., Mol., Opt. Phys.* **1979**, *19*, 920−922.

(99) Argenti, L.; Moccia, R. *J. Phys. B: At., Mol. Opt. Phys.* **2006**, *39*, 2773−2790.

(100) Mourik, T. V.; Wilson, A. K.; Dunning, T. H., Jr. *Mol. Phys.* **1999**, *96*, 529−547.

(101) Herrick, D. R. Doubly Excited Two-Electron Atoms. In *New Symmetry Properties of Atoms and Molecules*; Prigogine, I., Rice, S. A., Eds.; Advances in Chemical Physics; John Wiley & Sons: New York, 1983; Vol. 52, pp 27−69, DOI: 10.1002/9780470142769.ch1.

(102) Dunning, T. H. *J. Chem. Phys.* **1989**, *90*, 1007.

(103) Fojón, O. a.; Fernández, J.; Palacios, A.; Rivarola, R. D.; Martín, F. *J. Phys. B: At., Mol. Opt. Phys.* **2004**, *37*, 3035−3042.

(104) Sánchez, I.; Martín, F. *Phys. Rev. A: At., Mol., Opt. Phys.* **1998**, *57*, 1006−1017.